mTOR Controls Mitochondrial Dynamics and Cell Survival via MTFP1

Masahiro Morita[1,2,11], Julien Prudent[3,4,11], Kaustuv Basu[5], Vanessa Goyon[3], Sakie Katsumura[2], Laura Hulea[6,7], Dana Pearl[1], Nadeem Siddiqui[1], Stefan Strack[8], Shawn McGuirk[1], Julie St-Pierre[1], Ola Larsson[9], Ivan Topisirovic[1,6,7], Hojatollah Vali[5], Heidi M. McBride[3,*], John J. Bergeron[10,*], Nahum Sonenberg[1,12,*]

[1]Department of Biochemistry and Goodman Cancer Research Centre, McGill University, Montreal, QC H3A1A3, Canada

[2]Department of Molecular Medicine and Barshop Institute of Longevity and Aging Studies, University of Texas Health San Antonio, San Antonio, TX 78229, USA

[3]Montreal Neurological Institute, McGill University, Montreal, QC H3A 2B4, Canada

[4]Medical Research Council Mitochondrial Biology Unit, University of Cambridge, Wellcome Trust/MRC building, Cambridge Biomedical Campus, Hills Road, Cambridge CB2 0XY, UK

[5]Department of Anatomy & Cell Biology, McGill University, Montreal, QC H3A 0C7, Canada

[6]Lady Davis Institute, SMBD JGH, McGill University, Montreal, QC H3T 1E2, Canada

[7]Department of Oncology, McGill University, Montreal, QC H3T 1E2, Canada

[8]Department of Pharmacology, University of Iowa, Iowa city, IA 52242, USA

[9]Department of Oncology-Pathology, Karolinska Institutet, Stockholm 171 76, Sweden

[10]Department of Medicine, McGill University Health Centre Research Institute, Montreal, QC H4A 3J1, Canada

[11]Co-first author

[12]Lead contact

*Correspondence: heidi.mcbride@mcgill.ca (H.M.M.), john.bergeron@mcgill.ca (J.J.B.), nahum.sonenberg@mcgill.ca (N.S.)

ABSTRACT

The mechanisms that link environmental and intracellular stimuli to mitochondrial functions, including fission and fusion, ATP production, metabolite biogenesis and apoptosis, are not well understood. Here, we demonstrate that the nutrient-sensing mechanistic/mammalian target of rapamycin complex 1 (mTORC1) stimulates translation of mitochondrial fission process 1 (MTFP1) protein to control mitochondrial fission and apoptosis. Expression of MTFP1 is coupled to pro-fission phosphorylation and mitochondrial recruitment of the fission GTPase, dynamin-related protein 1 (DRP1). Potent active-site mTOR inhibitors engender mitochondrial hyperfusion due to the diminished translation of MTFP1 mediated by the translation initiation factor 4E (eIF4E)-binding proteins (4E-BPs). Uncoupling MTFP1 levels from the mTORC1/4E-BP pathway upon mTOR inhibition blocks the hyperfusion response and leads to apoptosis by converting mTOR inhibitor action from cytostatic to cytotoxic. These data provide direct evidence for the survival function of mitochondrial hyperfusion upon mTOR inhibition by employing MTFP1 as a critical effector of mTORC1 to govern cell fate decisions.

INTRODUCTION

The mechanistic/mammalian target of rapamycin (mTOR) integrates extracellular signals and intracellular cues (e.g. growth factors, insulin, nutrients and oxygen) to stimulate anabolism (e.g. protein and lipid synthesis) and bolster cellular growth and proliferation while suppressing catabolic processes (e.g. autophagy) (Efeyan et al., 2015; Laplante and Sabatini, 2012; Shimobayashi and Hall, 2014). mTOR is the catalytic subunit of two functionally distinct complexes named mTOR Complex 1 (mTORC1) and 2 (mTORC2) (Hara et al., 2002; Kim et al., 2002; Sarbassov et al., 2004). mTORC1 is activated by growth factors and insulin via the PI3K-AKT-TSC1/2 pathway and by amino acids via RAG small GTPases (Laplante and Sabatini, 2012; Zoncu et al., 2011). mTORC1 stimulates mRNA translation and other anabolic processes (e.g., lipid and nucleotide syntheses), but suppresses autophagy (Shimobayashi and Hall, 2014). mTORC2 controls cytoskeleton organization and cell survival by activating AGC kinase family members, and is implicated in regulating glucose and lipid metabolism (Laplante and Sabatini, 2012; Shimobayashi and Hall, 2014).

mTORC1 functions are mediated by multiple downstream effectors. Prominent ones include: translation initiation factor 4E (eIF4E)-binding proteins (4E-BPs), ribosomal S6 kinases (S6Ks) and UNC-51-like kinase 1 (ULK1) (Bhat et al., 2015). 4E-BPs are translation initiation repressors, which bind to the mRNA 5'cap-binding protein eIF4E and prevent the assembly of the eIF4F complex that facilitates ribosome recruitment to the mRNA during translation initiation (Pause et al., 1994; Sonenberg and Hinnebusch, 2009). Phosphorylation of 4E-BPs by mTORC1 results in their dissociation from eIF4E, thus allowing assembly of the eIF4F complex consisting of eIF4E, the DEAD box helicase eIF4A and the scaffold protein eIF4G, to promote translation initiation (Gingras et al., 1999).

mTORC1 activation promotes the recruitment of selected mRNAs, including those encoding nuclear-encoded mitochondrial proteins, to ribosomes (Gandin et al., 2016; Larsson et

al., 2012; Morita et al., 2013). Increased translation is documented for subunits of oxidative phosphorylation complex I, III and V, and mitochondrial ribosomal subunit proteins (Gandin et al., 2016; Larsson et al., 2012; Morita et al., 2013). Increased translation augments mitochondrial biogenesis, respiration and energy production to drive cell growth and proliferation (Gandin et al., 2016; Morita et al., 2013). Strikingly, the selected mRNAs also encode a protein relevant to mitochondrial fission, mitochondrial fission process protein 1 (MTFP1), also called MTP18. (Larsson et al., 2012).

MTFP1 is an integral protein of the mitochondrial inner membrane, whose loss results in a hyperfused mitochondrial reticulum, whereas its overexpression engenders fragmentation (Tondera et al., 2005; Tondera et al., 2004; Wai and Langer, 2016). MTFP1 activity in mitochondrial fission is mediated by the essential fission GTPase, dynamin-related protein 1 (DRP1) (Tondera et al., 2005). Previous studies have established that mitochondria hyperfuse upon nutrient deprivation through the PKA-dependent phosphorylation of DRP1, which blocks DRP1 recruitment to mitochondria (Gomes et al., 2011; Rambold et al., 2011). However, links to mTORC1 signaling were not examined, and the functional significance of hyperfusion under these conditions remains unknown.

In this study, we demonstrate that mTORC1 stimulates mitochondrial fission via 4E-BP-mediated translational regulation of the mitochondrial fission factor, MTFP1. Suppression of mTORC1 activity by pharmacological or genetic means causes mitochondrial hyperfusion, branching and circularization. This is a consequence of downregulation of MTFP1 levels via the mTORC1/4E-BP pathway, thereby eliciting changes in phosphorylation and localization of the mitochondrial fission factor DRP1. Notably, the disruption of this mechanism upon mTOR inhibition results in cell death. Our results unveil a previously unknown signaling pathway that links the sensing of physiological stimuli by mTORC1 with mitochondrial morphology and cell survival.

RESULTS

Active-site mTOR inhibitor induces mitochondrial hyperelongation and branching

mTORC1 stimulates mitochondrial functions including respiration, the TCA cycle and biogenesis (Cunningham et al., 2007; Morita et al., 2013; Schieke et al., 2006), and enhances translation of selected mRNAs encoding mitochondrial proteins (Gandin et al., 2016; Larsson et al., 2012; Morita et al., 2013). Mitochondrial functions are linked to mitochondrial dynamics of fission and fusion (Friedman and Nunnari, 2014; Wai and Langer, 2016). To investigate whether the nutrient-sensing mTORC1 pathway affects mitochondrial dynamics, we first examined mitochondrial morphology in cells treated with an active-site mTOR inhibitor (asTORi) (Figures 1, 2, S1 and S2). Using Transmission Electron Microscopy (TEM), we observed that the asTORi Ink1341-treated mouse embryonic fibroblasts (MEFs) displayed exaggerated mitochondrial elongation, branching and circularization as compared to vehicle-treated cells (Figures 1A and 1B, quantification in 1C-H). Quantitative analysis revealed that over 20% of mitochondria were elongated in asTORi-treated cells (> 2 μm in length, 4% in vehicle control) (Figures 1C and 1H). asTORi-treated cells also showed mitochondrial branching, with 9% of mitochondria identified as branched, which was very rarely observed in vehicle-treated cells (Figure 1D). Total mitochondrial number and area per cytoplasmic area were decreased (by 27%) by asTORi as compared to control (Figures 1E and 1F). As reported previously (Sini et al., 2010; Thoreen et al., 2009), asTORi stimulated autophagosome formation (Figures 1B and 1G). The effect of the allosteric inhibitor of mTORC1, rapamycin, on mitochondrial dynamics was also tested (Figures S1A-D). Rapamycin-treated cells displayed significant mitochondrial elongation compared to vehicle-treated cells (Figures S1A-D). In contrast to asTORi, quantitative analysis revealed that the effect of the rapamycin on mitochondrial morphology is milder than asTORi. Indeed, only 6% of mitochondria were elongated (> 2 μm in length) in rapamycin-treated cells as compared to asTORi-treated cells (20%) (Figures S1D compared to 1H). Furthermore, rapamycin treatment rarely induced

mitochondrial branching (Figure S1C), which was observed in asTORi-treated cells (Figure 1D). Rapamycin decreased mitochondrial number per cytoplasmic area and promoted autophagosome formation (Figure S1C).

To analyze the 3-D architecture of elongated mitochondria, Focused Ion Beam-Scanning Electron Microscopy (FIB-SEM) of 30 consecutive serial sections was performed (Figures 1I-J, S2A-B, and Movies S1-2). asTORi-treated cells exhibited elongation beyond 10 μm with many branch points that led to circularization of mitochondria, which were not seen in vehicle-treated cells (Figures 1I-J, S2A-B and Movies S1-2). Cristae architecture appeared intact with no significant alterations. Confocal microscopy further corroborated the fused and branched mitochondrial phenotype seen in asTORi-treated cells relative to vehicle control (Figures 2A and 2B). Mitochondria were elongated in more than 60% of cells treated with asTORi (Figure 2B). The hyperfusion and branching of mitochondria upon selective inhibition of mTOR provide strong evidence that mitochondrial dynamics are regulated by the mTOR signaling pathway.

asTORi alters DRP1 localization and phosphorylation, and protein levels of the mitochondrial fission factor, MTFP1

Mitochondrial fission is initiated by recruitment of the key fission factor DRP1 to mitochondria (Friedman and Nunnari, 2014; Wai and Langer, 2016). Confocal microscopy demonstrated that asTORi reduced DRP1 foci along the mitochondrial tubules (Figure 2C). This result was confirmed by subcellular fractionation analysis of DRP1 protein (Figure 2D). We thus assessed the effect of asTORi on levels and modifications of mitochondrial fission/fusion factors. A time course analysis of the changes in mitochondrial fission/fusion proteins over a 24 hr period in the presence of asTORi showed a 7-fold increase in phosphorylation of DRP1 at Ser 637 (S637) as compared to control (Figure 2E, and quantification in Figure S2C). Phosphorylation of DRP1 at S637 prevents its translocation to the mitochondria (Cereghetti et al., 2008; Chang and

7

Blackstone, 2007; Cribbs and Strack, 2007). Conversely, the pro-fission phosphorylation site of DRP1 at Ser 616 (S616) (Qi et al., 2011; Taguchi et al., 2007; Yu et al., 2011) was decreased in asTORi-treated cells (Figure 2E, and quantification in Figure S2C). While total DRP1 was slightly reduced in asTORi-treated cells, there was a significant reduction (60%) in the mitochondrial fission protein, MTFP1 (Figure 2E, and quantification in Figure S2C), whose mRNA translation was reported to be suppressed by asTORi in a genome-wide interrogation of the translatome (Larsson et al., 2012). In contrast, the levels of the mitochondrial fission factor (MFF) and the fusion GTPases, mitofusin 2 (MFN2) and optic atrophy 1 (OPA1) were not affected by asTORi (Figure 2E). As reported (Feldman et al., 2009; Thoreen et al., 2009; Yu et al., 2009), asTORi abolished the phosphorylation of 4E-BP1 and S6K1, and led to a reduction in LC3-I (cytoplasmic form) levels and an increase in LC3-II (membrane-bound lipidated form) (Figure 2E, and quantification in Figure S2C), confirming the induction of autophagy (Figure 1G). Compared to asTORi, including Ink1341 and Torin1, rapamycin exerted a lesser effect on DRP1 phosphorylation at S616 and S637 and no effect on MTFP1 protein levels (Figure S1E). In agreement with previous reports (Feldman et al., 2009; Thoreen et al., 2009), rapamycin and asTORi inhibited the S6K1 phosphorylation to the same extent, but rapamycin only partially inhibited the 4E-BP1 phosphorylation (Figure S1E), indicating that the differential effects of rapamycin and asTORi on mitochondrial dynamics depends on 4E-BPs. Thus, asTORi affects DRP1 phosphorylation and reduces expression of MTFP1, without major alterations in levels of other mitochondrial fission/fusion factors.

mTORC1, but not mTORC2, induces mitochondrial fragmentation

asTORi inhibits both mTORC1 and mTORC2 (Benjamin et al., 2011). To determine which mTOR complex controls mitochondrial fission, mitochondrial morphology was examined in MEFs lacking either raptor or rictor (Cybulski et al., 2012), which are subunits of mTORC1 and

mTORC2, respectively (Figures 3A-C and S3A-B). In raptor knockout (KO) MEFs, over 50% of cells exhibited mitochondrial elongation, whereas there was no change in mitochondrial morphology in rictor KO cells (Figures 3A-C and S3A-B). Reduced recruitment of DRP1 to mitochondria was also evident in raptor, but not rictor KO cells (Figures 3A-B). DRP1 phosphorylation at S616 was decreased, and the inhibitory S637 phosphorylation increased by raptor deletion (Figure 3D, quantification in Figure S3C). The total amount of DRP1 was mildly reduced (21%) in raptor-deleted cells (Figure 3D, quantification in Figure S3C), as compared to asTORi treatment (Figure 2D). MTFP1 protein level was decreased by 40% upon raptor deletion (Figure 3D, quantification in Figure S3C). Raptor KO had no effect on protein levels of the mitochondrial fusion factor, OPA1 (Figure 3D). In sharp contrast to raptor, rictor deletion had no effect on the levels of mitochondrial fission factors, DRP1 and MTFP1 (Figure 3E, quantification in Figure S3C). S6K1 and 4E-BP1 phosphorylation was decreased in raptor, but not in rictor KO MEFs (Figures 3D-E). These data demonstrate that mTORC1, but not mTORC2, mediates the effect of asTORi on expression of mitochondrial fission factors and mitochondrial morphology.

To corroborate the role of mTORC1 in mitochondrial fission, we employed TSC2 KO cells in which mTORC1 is constitutively active (Zhang et al., 2003). As reported (Jaeschke et al., 2002; Zhang et al., 2003), TSC2 KO MEFs exhibited elevated phosphorylation of 4E-BP1 and S6K1 as compared to wild-type (WT) MEFs (Figure 4A). An increase in DRP1 phosphorylation on S616, a decrease on S637 and an increase in DRP1 and MTFP1 protein levels were observed in TSC2 KO relative to WT (Figure 4A, quantification in Figure S3D). Consistently, loss of TSC2 promoted mitochondrial fission (Figures 4B and 4C). Mitochondria were fragmented in 38% of TSC2 KO cells (Figure 4C). These results further support the conclusion that mTORC1 drives mitochondrial fragmentation by controlling the mitochondrial fission factors including DRP1 and MTFP1.

4E-BPs are required for the mTORC1-dependent regulation of mitochondrial structure and the asTORi-induced translational arrest of *Mtfp1* mRNA

The above described data documented the effects of the mTORC1 pathway on two branches of the mitochondrial division machinery; first through the regulation of DRP1 phosphorylations, and second through the reduction in MTFP1. We have previously identified mRNAs whose translation is selectively suppressed by mTOR inhibition using genome-wide polysome profiling (Larsson et al., 2012). Among the suppressed mRNAs was the fission factor, MTFP1. 4E-BPs are major mediators of mTORC1-dependent regulation of mRNA translation (Sonenberg and Hinnebusch, 2009). To investigate the contribution of selective regulation of mRNA translation to mitochondrial hyperfusion, we examined the effects of asTORi in MEFs lacking 4E-BP1 and 4E-BP2 (Petroulakis et al., 2009). These cells are devoid of the three 4E-BPs, as MEFs do not express 4E-BP3 (Dowling et al., 2010). In striking contrast to the results obtained in WT MEFs (Figure 1), the effect of asTORi on mitochondrial branching was abolished and hyperfusion was significantly reduced in 4E-BP1 and 4E-BP2 double knockout (4E-BP DKO) MEFs, as determined by TEM (Figures 5A-F and S4A-D). 7% of mitochondria were elongated (> 2 μm in length) in 4E-BP DKO cells treated with asTORi (as compared to 20% in asTORi-treated WT cells), which was comparable to what was observed in vehicle-treated cells (Figures 5C and S4D). In contrast to WT MEFs, branched mitochondria were rarely observed in 4E-BP DKO cells treated with asTORi (9% vs 1% for 4E-BP WT and DKO, respectively) (Figure 5D), whereas autophagosome formation was induced by asTORi in both cells (Figure 5F). Confocal microscopy confirmed that deletion of 4E-BPs reversed the effect of asTORi on mitochondrial elongation (Figure 5G). Furthermore, DRP1 association with mitochondria was unaltered by asTORi in 4E-BP DKO MEFs (Figure 5H), in sharp contrast to WT MEFs (Figure 2C). Hence, the effect of mTORC1 on mitochondrial morphology is mediated by 4E-BPs.

We have verified the translational suppression of *Mtfp1* mRNA by asTORi PP242 (38% decrease) (Figure S4E), whereas no significant change (FDR > 0.05) in *Drp1* mRNA translation was observed (Larsson et al., 2012). This result was also confirmed using polysome profiling in Ink1341-treated cells (Figures 6A and 6B). Ink1341 inhibited global mRNA translation in WT MEFs, as illustrated by a decrease in heavy polysome fractions with a concomitant increase in the 80S peak (Figure 6A). Consistent with a reduction in MTFP1 protein in asTORi-treated cells (Figure 2E), asTORi inhibited the translation of *Mtfp1* mRNA, as illustrated by a shift of this mRNA toward lighter fractions (Figure 6B). As reported previously (Dowling et al., 2010), *cyclin D3* mRNA was shifted to light polysomes by asTORi, while *β-actin* mRNA was not (Figure 6B). *Mtfp1* mRNA levels were not altered by asTORi treatment (Figure S4F). These data further demonstrate that mTORC1 regulates MTFP1 expression at the level of translation.

In 4E-BP DKO MEFs, asTORi impaired global polysome formation to a lower extent as compared to their WT counterparts, as illustrated by a smaller increase in the 80S monosomes peak and a decrease in polysomes (compare Figures 6C to 6A). asTORi failed to induce a shift of *Mtfp1* and *Cyclin D3* mRNAs toward lighter fractions in 4E-BP DKO cells (Figure 6D), indicating that 4E-BPs repress translation of these mRNAs. Accordingly, the suppression of MTFP1 protein expression by asTORi observed in WT cells was attenuated in 4E-BP DKO MEFs (Figure 6E, quantification in Figure S4G). The deletion of 4E-BPs reversed the effects of asTORi on DRP1 S616 and S637 phosphorylation (Figure 6E, quantification in Figure S4G).

Translational activity of eIF4E is regulated through interaction with 4E-BPs as well as eIF4E phosphorylation induced by the MAPK/MNK signaling pathway (Bhat et al., 2015; Topisirovic et al., 2004). To further study the role of the 4E-BP/eIF4E axis in mitochondrial dynamics, we treated WT MEFs with phorbol 12-myrustate 13-acetate (PMA) that activates the MAPK pathway and enhances eIF4E phosphorylation (Goto et al., 2009) (Figures S5A-C). PMA-treatment induced an increase in DRP1 S616 phosphorylation and DRP1 and MTFP1 protein levels

11

with a concomitant decrease in S637 phosphorylation (Figure S5A), and correlated with a strong mitochondrial fragmentation phenotype (70% of cells with fragmented mitochondria in PMA-treatment compared to 20% in controls) (Figures S5B and S5C).

To show that the role of the mTORC1/4E-BP axis in mitochondrial dynamics is not restricted to MEFs, we examined the effect of asTORi treatment on A375 human malignant melanoma 4E-BP1/2 WT and DKO cells, engineered by the CRISPR technology (Figures S5D-F). Compared to 4E-BP DKO A375 cells, WT A375 cells treated with asTORi exhibited a significant increase of mitochondrial hyperfusion correlated to a decrease in levels of MTFP1 protein and DRP1(S616) phosphorylation (Figures S5D-F), phenocopying asTORi-treated WT MEFs (Figures 2A, 2B and 2E). In conclusion, 4E-BPs function as mediators of mTORC1 on downstream mitochondrial fission through the translational control of the mRNA encoding the mitochondrial fission protein, MTFP1.

MTFP1 is the major mediator of the mTORC1/4E-BP-directed control of mitochondrial morphology

The mitochondrial elongation phenotype observed as a result of asTORi treatment is characterized by an 4E-BP-dependent decrease of the MTFP1 protein level and an alteration of the S616 and S637 DRP1 phosphorylation. To elucidate the relationship and chronology of these two phenomena, rescue experiments were performed in MEFs treated with asTORi that expressed phospho-DRP1 mutants fused with GFP (Figure S6A-D). Cells transiently expressing GFP-DRP1-WT, GFP-DRP1-S616D (phospho-mimetic mutant), GFP-DRP1-S637A (non-phosphorylatable mutant) and double GFP-DRP1-S616D/S637A were treated with asTORi or vehicle for 24 hr (Figure S6B), and mitochondrial morphology was analyzed by confocal microscopy (Figures S6C and S6D). All GFP-DRP1 mutants were well expressed (Figures S6A and S6B) with GFP1-DRP1-637A and GFP-DRP1-S616D/S637A localized to mitochondria and leading to mitochondrial

12

fragmentation (Figure S6C and S6D). However, the DRP1 mutants only partially rescued (20%) the mitochondrial hyperfusion induced by asTORi (control cells treated with asTORi presented 65% of elongated mitochondria compared to 46%, 46%, 41% and 40% for GFP-DRP1-WT, GFP-DRP1-S616D, GFP-DRP1-S637A and GFP-DRP1-S616D/S637A, respectively) (Figures 2A-B and S6C-D).

We therefore wished to determine whether translational suppression of the fission factor, MTFP1, underlies the effect of the mTORC1/4E-BP axis on mitochondrial fission. We rescued the expression of MTFP1 using a construct lacking the mRNA 5'UTR that is translationally sensitive to mTOR inhibition (Thoreen et al., 2012), to render its translation 4E-BP-independent (Figure 7A). Accordingly, asTORi reduced MTFP1 protein levels in control, but not in cells expressing the mutant MTFP1, while 4E-BP1 phosphorylation was suppressed equally in both cells (Figure 7A). MTFP1 expression stabilized the pro-fission S616 phosphorylation of DRP1, and reduced S637 phosphorylation in the presence of asTORi (Figure 7A, quantification in Figure S7A). Consistent with a previous report (Tondera et al., 2005), expression of MTFP1 increased mitochondrial fragmentation (Figures 7B and 7C). Importantly, compared to DRP1-mutants, MTFP1 re-expression fully blocked the mitochondrial hyperfusion induced by asTORi (Figures 7B and 7C). Similar rescue experiments were performed in raptor KO cells (Figures S7B-D), where overexpression of MTFP1 induced mitochondrial fragmentation (Figures S7C and S7D) and rescued both the mitochondrial elongation and the decrease in DRP1 S616 phosphorylation observed in raptor KO cells (Figures S7B-D).

Finally, to confirm that the increased expression of MTFP1 was responsible for the fragmented mitochondrial phenotype in the mTORC1 signaling-activated cells (Figures 4 and S3D), knockdown of MTFP1 by siRNA was performed (Figure S7E-G). MTFP1 silencing significantly induced mitochondrial hyperfusion in both TSC2 WT and KO MEF cells (Figures S7F and S7G), accompanied by a decrease in the phosphorylation of DRP1 at S616 (Figure S7E).

13

These data demonstrate that the loss of MTFP1 is responsible for the drastic mitochondrial hyperfusion seen upon inhibition of the mTORC1/4E-BP signaling pathway.

asTORi-induced loss of MTFP1 protects cells from death

The observation that mTOR inhibition leads to mitochondrial hyperfusion could provide an explanation for the cytostatic action of mTOR inhibitors (Benjamin et al., 2011). It has previously been suggested that the induction of mitochondrial hyperfusion during starvation renders mitochondria refractive to autophagy and protects cells against apoptosis (Gomes et al., 2011). We therefore employed the rescue of MTFP1 expression to examine the functional contribution of mitochondrial hyperfusion to asTORi action. asTORi Ink1341 and Ink128 dramatically reduced proliferation of cells expressing *Mtfp1* mRNA, which is refractory to 4E-BP-dependent translational regulation, as compared to control cells (Figures 7D and 7E). The re-expression of 4E-BP-refractory MTFP1 induced poly (ADP-ribose) polymerase (PARP) cleavage (Figure S7H) and enhanced caspase-3/7 activity (Figure 7F), both hallmark phenomena of apoptosis, after 48 hr of treatment with asTORi. These data demonstrate that the impairment of mitochondrial hyperfusion caused by uncoupling of MTFP1 expression from the mTORC1/4E-BP pathway converts asTORi action from cytostatic to cytotoxic, which could be exploited to improve the anti-neoplastic efficacy of mTOR inhibitors in the clinic.

DISCUSSION

We demonstrate that asTORi treatment leads to dramatic mitochondrial branching and hyperfusion specifically mediated through the mTORC1/4E-BP/MTFP1 axis. Indeed, asTORi can target mTORC1 and mTORC2; however, the use of raptor and rictor KO MEFs clearly determine that mTORC1 is solely responsible for our phenotype (Figure 3). Moreover, the 4E-BPs deletion reverses mitochondrial hyperfusion and down-regulation of *Mtfp1* mRNA translation induced by asTORi (Figures 5 and 6). The specificity of the mTORC1/4E-BP has been confirmed by the magnitude of the effects of asTORi and rapamycin treatments. Indeed, we show that asTORi leads to a more dramatic mitochondrial elongation than rapamycin (Figures 1, 2, S1 and S2). In both treatments, DRP1 phosphorylation states are altered to a lesser extent in rapamycin, and rapamycin does not decrease the MTFP1 protein level most probably due to the lack of 4E-BP1 phosphorylation inhibition as reported previously (Feldman et al., 2009; Thoreen et al., 2009). Furthermore, the 4E-BP/eIF4E axis was reported to modulate translation of a series of mTORC1-sensitive mRNAs encoding proliferation- and survival-promoting proteins (e.g., cyclins, BCL-2, MCL-1 and MYC) (Dowling et al., 2010; Gandin et al., 2016; Larsson et al., 2007; Larsson et al., 2012), indicating that 4E-BPs contribute to cell survival upon mTOR inhibition via several target mRNAs. Our findings suggest that concomitant inhibition of the mTORC1 activity and mitochondrial fusion may be used to increase cytotoxicity and the anti-neoplastic efficacy of mTOR inhibitors in the clinic.

MTFP1 is a critical regulator of DRP1 phosphorylation downstream of the mTORC1 signaling pathway. Accordingly, rescue of MTFP1 expression in asTORi-treated, raptor KO and TSC2 KO cells completely reverses both mitochondrial morphology and DRP1 phosphorylation states (Figures 7 and S7), whereas expression of phospho-DRP1 mutants partially rescues mitochondrial elongation (Figure S6). These results underscore the central role of MTFP1 in the control of mitochondrial dynamics upstream of DRP1 during mTOR inhibition; however, how

15

MTFP1, an inner mitochondrial membrane protein, controls DRP1 phosphorylation is an open question. The data imply a retrograde signaling pathway between MTFP1 and the kinases that phosphorylate DRP1 to regulate fission. MTFP1 is an integral inner membrane protein of 18 kDa with no known function (Tondera et al., 2005). Interestingly, it was recently established that at least one key signal for mitochondrial division is the local replication of mtDNA (Lewis et al., 2016; Murley et al., 2013). mtDNA is packaged within nucleoids, and nucleoids with newly replicated DNA mark the sites of contact with the ER, leading to fission and successful segregation of the mitochondrial genomes (Murley et al., 2013). Whether MTFP1 participates in this signaling process is unclear. However, it is noteworthy that a major component of mtDNA nucleoids, transcription factor A, mitochondrial (TFAM) is also a selective target of 4E-BP-mediated translation, suggesting that these components may function in a common pathway targeted by mTOR (Morita et al., 2013). Regardless of the precise mechanism, our data establish MTFP1 as an essential regulator of mitochondrial fission through the modulation of DRP1 phosphorylation and recruitment. The S616 phosphorylation of DRP1 is controlled by many kinases that depend on the cellular context, most notably ERK1/2 within RAS-induced tumors (Kashatus et al., 2015; Prudent and McBride, 2017; Serasinghe et al., 2015). mTORC1 signaling, which is aberrantly activated in many cancers, has also been linked to the ERK1/2 kinases (Chen et al., 2010; Mendoza et al., 2011). Further work will focus on identifying the molecular signals that link MTFP1 function within the inner membrane and the kinases that regulate phosphorylation of DRP1 downstream of the mTORC1/4E-BP/MTFP1 axis.

Mitochondrial morphology varies across cell types and tissues in physiological and pathological conditions (Friedman and Nunnari, 2014; Vyas et al., 2016). A major challenge has been to understand the molecular mechanisms that couple intracellular and environmental stimuli to mitochondrial dynamics. asTORi treatment induced a mitochondrial elongation phenotype, similar to what occurs during starvation (Gomes et al., 2011; Rambold et al., 2011). We previously

characterized a series of specific 4E-BP specific targets that function to lower mitochondrial metabolism, including reductions in components of the ETC and ATP synthase, subunits of the mitochondrial ribosome, TFAM and others (Morita et al., 2013). In addition, those studies revealed a nearly 40% reduction in mtDNA levels upon asTORi treatment. Together with evidence presented here revealing a direct link to mitochondrial morphology and survival, this underscores mitochondrial metabolism as a major target of the adaptive response to mTOR inhibition. This is in sharp contrast to response seen upon mitochondrial dysfunction, where fragmentation and mitophagy are fully activated (Toyama et al., 2016). Precipitous reductions in cellular ATP through inhibition of the ETC was recently shown to damage mitochondria and activate AMP-activating protein kinase (AMPK), leading to direct phosphorylation of the DRP1 receptor MFF (Toyama et al., 2016). This resulted in highly fragmented mitochondria, which were then cleared by mitophagy (Toyama et al., 2016). Indeed, mitochondrial damage is a requisite for stalled PINK1 import, Parkin recruitment and mitophagy (Pickrell and Youle, 2015). Our data show that inhibition of mTORC1 does not trigger mitochondrial dysfunction directly, explaining why mitophagy is not programmed in this pathway.

mTOR signaling is hyper-activated in many cancers and promotes growth and proliferation (Benjamin et al., 2011; Bhat et al., 2015; Kim et al., 2016; Zoncu et al., 2011); thus, asTORi are currently being tested in phase I/II clinical trials (Basu et al., 2015; Bendell et al., 2015; Naing et al., 2012). A major challenge concerning the therapeutic inhibition of mTOR is the potential for compensatory mechanisms that increase survival of cancer cells (Benjamin et al., 2011). In this study, we provide evidence that the suppression of mTORC1 activity by active-site inhibitors reduces the translation of MTFP1, leading to the altered phosphorylation and localization of DRP1, a marked hyperfusion response and enhanced cell survival. Hence, the well-established anti-proliferative effects of asTORi are compensated by a protective effect of cell survival through reduction in MTPF1 levels. Importantly, uncoupling MTFP1 levels from the 4E-

BP-mediated regulation upon mTOR inhibition leads to apoptosis (Figure 7), demonstrating that translational control of MTFP1 by mTORC1/4E-BP acts as a critical determinant of cell fate. mTOR inhibitors are generally cytostatic and thus cannot be expected to act as potent anti-cancer drugs. Our results offer a new therapeutic strategy to maintain the pro-fission state in asTORi-based therapy, and thus promote cancer cell death.

STAR METHODS

Detailed methods are provided in the online version of this paper and include the following:

- KEY RESOURCES TABLE
- CONTACT FOR REAGENT AND RESOURCE SHARING
- EXPERIMENTAL MODEL AND SUBJECT DETAILS
  - Cell Lines and Cell Culture Conditions
- METHOD DETAILS
  - Transmission Electron Microscopy
  - Focused Ion Beam-Scanning Electron Microscope
  - Immunofluorescence
  - mTOR inhibitors, lentivirus infection, siRNA and GFP-DRP1 plasmid transfection
  - CRISPR-mediated gene knockout
  - BrdU incorporation, Giemsa staining, caspase-3/7 activity assay
  - Cell lysis, Western blotting, antibodies
  - Polysome profiling, RNA isolation, RT-qPCR
- QUANTIFICATION AND STATISTICAL ANALYSIS
  - Quantification of Immunoblottings
  - Statistical analysis
- DATA AND SOFTWARE AVAILABILITY

SUPPLEMENTAL INFORMATION

Supplemental information includes eight figures, one table and two movies.

AUTHOR CONTRIBUTIONS

ACKNOWLEDGMENTS

REFERENCES

Basu, B., Dean, E., Puglisi, M., Greystoke, A., Ong, M., Burke, W., Cavallin, M., Bigley, G., Womack, C., Harrington, E.A.*, et al*. (2015). First-in-Human Pharmacokinetic and Pharmacodynamic Study of the Dual m-TORC 1/2 Inhibitor AZD2014. Clin Cancer Res *21*, 3412-3419.

Bendell, J.C., Kelley, R.K., Shih, K.C., Grabowsky, J.A., Bergsland, E., Jones, S., Martin, T., Infante, J.R., Mischel, P.S., Matsutani, T.*, et al*. (2015). A phase I dose-escalation study to assess safety, tolerability, pharmacokinetics, and preliminary efficacy of the dual mTORC1/mTORC2 kinase inhibitor CC-223 in patients with advanced solid tumors or multiple myeloma. Cancer *121*, 3481-3490.

Benjamin, D., Colombi, M., Moroni, C., and Hall, M.N. (2011). Rapamycin passes the torch: a new generation of mTOR inhibitors. Nature reviews. Drug discovery *10*, 868-880.

Bhat, M., Robichaud, N., Hulea, L., Sonenberg, N., Pelletier, J., and Topisirovic, I. (2015). Targeting the translation machinery in cancer. Nature reviews. Drug discovery *14*, 261-278.

Cereghetti, G.M., Stangherlin, A., Martins de Brito, O., Chang, C.R., Blackstone, C., Bernardi, P., and Scorrano, L. (2008). Dephosphorylation by calcineurin regulates translocation of Drp1 to mitochondria. Proceedings of the National Academy of Sciences of the United States of America *105*, 15803-15808.

Chang, C.R., and Blackstone, C. (2007). Cyclic AMP-dependent protein kinase phosphorylation of Drp1 regulates its GTPase activity and mitochondrial morphology. J Biol Chem *282*, 21583-21587.

Chen, X.G., Liu, F., Song, X.F., Wang, Z.H., Dong, Z.Q., Hu, Z.Q., Lan, R.Z., Guan, W., Zhou, T.G., Xu, X.M.*, et al*. (2010). Rapamycin regulates Akt and ERK phosphorylation through mTORC1 and mTORC2 signaling pathways. Mol Carcinog *49*, 603-610.

Cribbs, J.T., and Strack, S. (2007). Reversible phosphorylation of Drp1 by cyclic AMP-dependent protein kinase and calcineurin regulates mitochondrial fission and cell death. EMBO Rep *8*, 939-944.

Cunningham, J.T., Rodgers, J.T., Arlow, D.H., Vazquez, F., Mootha, V.K., and Puigserver, P. (2007). mTOR controls mitochondrial oxidative function through a YY1-PGC-1alpha transcriptional complex. Nature *450*, 736-740.

Cybulski, N., Zinzalla, V., and Hall, M.N. (2012). Inducible raptor and rictor knockout mouse embryonic fibroblasts. Methods Mol Biol *821*, 267-278.

Dowling, R.J., Topisirovic, I., Alain, T., Bidinosti, M., Fonseca, B.D., Petroulakis, E., Wang, X., Larsson, O., Selvaraj, A., Liu, Y., *et al*. (2010). mTORC1-mediated cell proliferation, but not cell growth, controlled by the 4E-BPs. Science *328*, 1172-1176.

Efeyan, A., Comb, W.C., and Sabatini, D.M. (2015). Nutrient-sensing mechanisms and pathways. Nature *517*, 302-310.

Feldman, M.E., Apsel, B., Uotila, A., Loewith, R., Knight, Z.A., Ruggero, D., and Shokat, K.M. (2009). Active-site inhibitors of mTOR target rapamycin-resistant outputs of mTORC1 and mTORC2. PLoS Biol *7*, e38.

Friedman, J.R., and Nunnari, J. (2014). Mitochondrial form and function. Nature *505*, 335-343.

Gandin, V., Masvidal, L., Hulea, L., Gravel, S.P., Cargnello, M., McLaughlan, S., Cai, Y., Balanathan, P., Morita, M., Rajakumar, A., *et al*. (2016). nanoCAGE reveals 5' UTR features that define specific modes of translation of functionally related MTOR-sensitive mRNAs. Genome Res *26*, 636-648.

Gandin, V., Sikstrom, K., Alain, T., Morita, M., McLaughlan, S., Larsson, O., and Topisirovic, I. (2014). Polysome fractionation and analysis of mammalian translatomes on a genome-wide scale. J Vis Exp *87*, e51455.

Gingras, A.C., Gygi, S.P., Raught, B., Polakiewicz, R.D., Abraham, R.T., Hoekstra, M.F., Aebersold, R., and Sonenberg, N. (1999). Regulation of 4E-BP1 phosphorylation: a novel two-step mechanism. Genes & development *13*, 1422-1437.

Gomes, L.C., Di Benedetto, G., and Scorrano, L. (2011). During autophagy mitochondria elongate, are spared from degradation and sustain cell viability. Nature cell biology *13*, 589-598.

Goto, S., Yao, Z., and Proud, C.G. (2009). The C-terminal domain of Mnk1a plays a dual role in tightly regulating its activity. The Biochemical journal *423*, 279-290.

Hara, K., Maruki, Y., Long, X., Yoshino, K., Oshiro, N., Hidayat, S., Tokunaga, C., Avruch, J., and Yonezawa, K. (2002). Raptor, a binding partner of target of rapamycin (TOR), mediates TOR action. Cell *110*, 177-189.

Jaeschke, A., Hartkamp, J., Saitoh, M., Roworth, W., Nobukuni, T., Hodges, A., Sampson, J., Thomas, G., and Lamb, R. (2002). Tuberous sclerosis complex tumor suppressor-mediated S6 kinase inhibition by phosphatidylinositide-3-OH kinase is mTOR independent. J Cell Biol *159*, 217-224.

Kashatus, J.A., Nascimento, A., Myers, L.J., Sher, A., Byrne, F.L., Hoehn, K.L., Counter, C.M., and Kashatus, D.F. (2015). Erk2 phosphorylation of Drp1 promotes mitochondrial fission and MAPK-driven tumor growth. Molecular cell *57*, 537-551.

Kim, D.H., Sarbassov, D.D., Ali, S.M., King, J.E., Latek, R.R., Erdjument-Bromage, H., Tempst, P., and Sabatini, D.M. (2002). mTOR interacts with raptor to form a nutrient-sensitive complex that signals to the cell growth machinery. Cell *110*, 163-175.

Kim, L.C., Cook, R.S., and Chen, J. (2016). mTORC1 and mTORC2 in cancer and the tumor microenvironment. Oncogene.

Laplante, M., and Sabatini, D.M. (2012). mTOR signaling in growth control and disease. Cell *149*, 274-293.

Larsson, O., Li, S., Issaenko, O.A., Avdulov, S., Peterson, M., Smith, K., Bitterman, P.B., and Polunovsky, V.A. (2007). Eukaryotic translation initiation factor 4E induced progression of primary human mammary epithelial cells along the cancer pathway is associated with targeted translational deregulation of oncogenic drivers and inhibitors. Cancer research *67*, 6814-6824.

Larsson, O., Morita, M., Topisirovic, I., Alain, T., Blouin, M.J., Pollak, M., and Sonenberg, N. (2012). Distinct perturbation of the translatome by the antidiabetic drug metformin. Proceedings of the National Academy of Sciences of the United States of America *109*, 8977-8982.

Lewis, S.C., Uchiyama, L.F., and Nunnari, J. (2016). ER-mitochondria contacts couple mtDNA synthesis with mitochondrial division in human cells. Science *353*, aaf5549.

Mali, P., Yang, L., Esvelt, K.M., Aach, J., Guell, M., DiCarlo, J.E., Norville, J.E., and Church, G.M. (2013). RNA-guided human genome engineering via Cas9. Science *339*, 823-826.

Mendoza, M.C., Er, E.E., and Blenis, J. (2011). The Ras-ERK and PI3K-mTOR pathways: cross-talk and compensation. Trends in biochemical sciences *36*, 320-328.

Morita, M., Gravel, S.P., Chenard, V., Sikstrom, K., Zheng, L., Alain, T., Gandin, V., Avizonis, D., Arguello, M., Zakaria, C., *et al*. (2013). mTORC1 controls mitochondrial activity and biogenesis through 4E-BP-dependent translational regulation. Cell metabolism *18*, 698-711.

Murley, A., Lackner, L.L., Osman, C., West, M., Voeltz, G.K., Walter, P., and Nunnari, J. (2013). ER-associated mitochondrial division links the distribution of mitochondria and mitochondrial DNA in yeast. Elife *2*, e00422.

Naing, A., Aghajanian, C., Raymond, E., Olmos, D., Schwartz, G., Oelmann, E., Grinsted, L., Burke, W., Taylor, R., Kaye, S., *et al*. (2012). Safety, tolerability, pharmacokinetics and pharmacodynamics of AZD8055 in advanced solid tumours and lymphoma. Br J Cancer *107*, 1093-1099.

Pause, A., Belsham, G.J., Gingras, A.C., Donze, O., Lin, T.A., Lawrence, J.C., Jr., and Sonenberg, N. (1994). Insulin-dependent stimulation of protein synthesis by phosphorylation of a regulator of 5'-cap function. Nature *371*, 762-767.

Petroulakis, E., Parsyan, A., Dowling, R.J., LeBacquer, O., Martineau, Y., Bidinosti, M., Larsson, O., Alain, T., Rong, L., Mamane, Y.*, et al*. (2009). p53-dependent translational control of senescence and transformation via 4E-BPs. Cancer cell *16*, 439-446.

Pickrell, A.M., and Youle, R.J. (2015). The roles of PINK1, parkin, and mitochondrial fidelity in Parkinson's disease. Neuron *85*, 257-273.

Prudent, J., and McBride, H.M. (2017). The mitochondria-endoplasmic reticulum contact sites: a signalling platform for cell death. Curr Opin Cell Biol *47*, 52-63.

Prudent, J., Zunino, R., Sugiura, A., Mattie, S., Shore, G.C., and McBride, H.M. (2015). MAPL SUMOylation of Drp1 Stabilizes an ER/Mitochondrial Platform Required for Cell Death. Molecular cell *59*, 941-955.

Qi, X., Disatnik, M.H., Shen, N., Sobel, R.A., and Mochly-Rosen, D. (2011). Aberrant mitochondrial fission in neurons induced by protein kinase C{delta} under oxidative stress conditions in vivo. Molecular biology of the cell *22*, 256-265.

Rambold, A.S., Kostelecky, B., Elia, N., and Lippincott-Schwartz, J. (2011). Tubular network formation protects mitochondria from autophagosomal degradation during nutrient starvation. Proceedings of the National Academy of Sciences of the United States of America *108*, 10190-10195.

Robitaille, A.M., Christen, S., Shimobayashi, M., Cornu, M., Fava, L.L., Moes, S., Prescianotto-Baschong, C., Sauer, U., Jenoe, P., and Hall, M.N. (2013). Quantitative phosphoproteomics reveal mTORC1 activates de novo pyrimidine synthesis. Science *339*, 1320-1323.

Sarbassov, D.D., Ali, S.M., Kim, D.H., Guertin, D.A., Latek, R.R., Erdjument-Bromage, H., Tempst, P., and Sabatini, D.M. (2004). Rictor, a novel binding partner of mTOR, defines a

rapamycin-insensitive and raptor-independent pathway that regulates the cytoskeleton. Current biology : CB *14*, 1296-1302.

Schieke, S.M., Phillips, D., McCoy, J.P., Jr., Aponte, A.M., Shen, R.F., Balaban, R.S., and Finkel, T. (2006). The mammalian target of rapamycin (mTOR) pathway regulates mitochondrial oxygen consumption and oxidative capacity. J Biol Chem *281*, 27643-27652.

Serasinghe, M.N., Wieder, S.Y., Renault, T.T., Elkholi, R., Asciolla, J.J., Yao, J.L., Jabado, O., Hoehn, K., Kageyama, Y., Sesaki, H., *et al*. (2015). Mitochondrial division is requisite to RAS-induced transformation and targeted by oncogenic MAPK pathway inhibitors. Molecular cell *57*, 521-536.

Shimobayashi, M., and Hall, M.N. (2014). Making new contacts: the mTOR network in metabolism and signalling crosstalk. Nature reviews. Molecular cell biology *15*, 155-162.

Sini, P., James, D., Chresta, C., and Guichard, S. (2010). Simultaneous inhibition of mTORC1 and mTORC2 by mTOR kinase inhibitor AZD8055 induces autophagy and cell death in cancer cells. Autophagy *6*, 553-554.

Sonenberg, N., and Hinnebusch, A.G. (2009). Regulation of translation initiation in eukaryotes: mechanisms and biological targets. Cell *136*, 731-745.

Taguchi, N., Ishihara, N., Jofuku, A., Oka, T., and Mihara, K. (2007). Mitotic phosphorylation of dynamin-related GTPase Drp1 participates in mitochondrial fission. J Biol Chem *282*, 11521-11529.

Thoreen, C.C., Chantranupong, L., Keys, H.R., Wang, T., Gray, N.S., and Sabatini, D.M. (2012). A unifying model for mTORC1-mediated regulation of mRNA translation. Nature *485*, 109-113.

Thoreen, C.C., Kang, S.A., Chang, J.W., Liu, Q., Zhang, J., Gao, Y., Reichling, L.J., Sim, T., Sabatini, D.M., and Gray, N.S. (2009). An ATP-competitive mammalian target of rapamycin inhibitor reveals rapamycin-resistant functions of mTORC1. J Biol Chem *284*, 8023-8032.

Tondera, D., Czauderna, F., Paulick, K., Schwarzer, R., Kaufmann, J., and Santel, A. (2005). The mitochondrial protein MTP18 contributes to mitochondrial fission in mammalian cells. J Cell Sci *118*, 3049-3059.

Tondera, D., Santel, A., Schwarzer, R., Dames, S., Giese, K., Klippel, A., and Kaufmann, J. (2004). Knockdown of MTP18, a novel phosphatidylinositol 3-kinase-dependent protein, affects mitochondrial morphology and induces apoptosis. J Biol Chem *279*, 31544-31555.

Topisirovic, I., Ruiz-Gutierrez, M., and Borden, K.L. (2004). Phosphorylation of the eukaryotic translation initiation factor eIF4E contributes to its transformation and mRNA transport activities. Cancer research *64*, 8639-8642.

Toyama, E.Q., Herzig, S., Courchet, J., Lewis, T.L., Jr., Loson, O.C., Hellberg, K., Young, N.P., Chen, H., Polleux, F., Chan, D.C., *et al*. (2016). Metabolism. AMP-activated protein kinase mediates mitochondrial fission in response to energy stress. Science *351*, 275-281.

Vyas, S., Zaganjor, E., and Haigis, M.C. (2016). Mitochondria and Cancer. Cell *166*, 555-566.

Wai, T., and Langer, T. (2016). Mitochondrial Dynamics and Metabolic Regulation. Trends Endocrinol Metab *27*, 105-117.

Yu, K., Toral-Barza, L., Shi, C., Zhang, W.G., Lucas, J., Shor, B., Kim, J., Verheijen, J., Curran, K., Malwitz, D.J., *et al*. (2009). Biochemical, cellular, and in vivo activity of novel ATP-competitive and selective inhibitors of the mammalian target of rapamycin. Cancer research *69*, 6232-6240.

Yu, T., Jhun, B.S., and Yoon, Y. (2011). High-glucose stimulation increases reactive oxygen species production through the calcium and mitogen-activated protein kinase-mediated activation of mitochondrial fission. Antioxid Redox Signal *14*, 425-437.

Zhang, H., Cicchetti, G., Onda, H., Koon, H.B., Asrican, K., Bajraszewski, N., Vazquez, F., Carpenter, C.L., and Kwiatkowski, D.J. (2003). Loss of Tsc1/Tsc2 activates mTOR and disrupts

PI3K-Akt signaling through downregulation of PDGFR. The Journal of clinical investigation *112*, 1223-1233.

Zoncu, R., Efeyan, A., and Sabatini, D.M. (2011). mTOR: from growth signal integration to cancer, diabetes and ageing. Nature reviews. Molecular cell biology *12*, 21-35.

FIGURE LEGENDS

Figure 1. Active-site mTOR inhibitor induces mitochondrial elongation, branching and circularization.

(A-B) Representative transmission electron microscopy (TEM) images of wild-type (WT) MEFs treated with vehicle (DMSO) (A) or Ink1341 (200 nM) (B) for 24 hr showing well-preserved mitochondria (Mito) and endoplasmic reticulum (ER) in (A), but elongated, branched and circularized mitochondria, ER and autophagosomes (AP) in (B). Scale bars represent 1 μm.

(C-H) Quantification of TEM images of WT MEFs treated with vehicle or Ink1341 for 24 hr showing mitochondrial length (C), percentage of branched mitochondria (D), mitochondrial number per 100 μm^2 of cytoplasmic area (E), mitochondrial area per cytoplasmic area (F), autophagosome area per cytoplasmic area (G) and distribution of mitochondrial length (H). Data are shown as 0 to 100% box plots with the 25th, 50th, and 75th percentiles as the lower, middle, and upper boundaries of the box, respectively. For (C, D, H), n = 1544 mitochondria for vehicle, n = 987 for Ink1341 from three independent experiments. For (E-G), n = 30 cells per group from three independent experiments. $*P < 0.05$, $**P < 0.01$, $***P < 0.001$; Student's t test.

(I-J) Focused Ion Beam-Scanning Electron Microscopy (FIB-SEM) 3-D visualization of WT MEFs treated with vehicle (I) or Ink1341 (200 nM) (J) for 24 hr showing mitochondria (Mito), ER and autophagosomes (AP). Scale bars represent 1 μm.

See also Figures S1 and S2.

Figure 2. Alterations in localization of DRP1 and protein levels of mitochondrial fission factors in asTORi-treated cells.

(A) Representative confocal images of mitochondrial morphology in wild-type (WT) MEFs treated with vehicle or Ink1341 (200 nM) for 24 hr. Mitochondria were labeled using an anti-TOM20 antibody. * indicates cells with elongated/branched mitochondria. Scale bars represent 20 μm.

(B) Quantification of mitochondrial morphology in WT MEFs treated with vehicle or Ink1341 (200 nM) for 24 hr (left). n = 303 for vehicle, n = 261 for Ink1341 from three independent experiments. Data represent mean ± SD. ***P < 0.001; Student's t test. Representative confocal images of cells with the indicated mitochondria (right).

(C) Representative images of mitochondrial morphology and DRP1 localization in MEFs treated with vehicle (upper) or Ink1341 (lower) for 24 hr. Mitochondria and DRP1 were stained with anti-TOM20 and anti-DRP1 antibodies, respectively. Scale bars represent 10 μm.

(D) Levels of DRP1, TOM20 and α-tubulin proteins in subcellular fractions from MEFs treated with vehicle or Ink1341 (200 nM) for 24 hr. Total cell lysates (Total) were fractionated into mitochondrial (Mito) and cytosolic (Cyto) fractions.

(E) Levels of proteins relevant to mitochondrial fission and fusion, mTORC1 signaling and autophagy in MEFs treated with Ink1341 (200 nM) for the indicated time. α-tubulin and β-actin were used as loading controls. Quantification of levels of the indicated proteins is shown in Figure S2C.

See also Figures S1 and S2.

Figure 3. mTORC1-dependent regulation of mitochondrial dynamics.

(A-B) Representative images of mitochondrial morphology and DRP1 localization in raptor wild-type (WT) and knockout (KO) MEFs (A), or rictor WT and KO MEFs (B). Mitochondria and DRP1 were stained with anti-TOM20 and anti-DRP1 antibodies, respectively. Scale bars represent 10 μm.

(C) Quantification of mitochondrial morphology in raptor WT and KO MEFs, or rictor WT and KO MEFs. n = 322 for raptor WT, n = 290 for raptor KO, n = 247 for rictor WT, n = 266 for rictor KO from three independent experiments. Data represent mean ± SD. **P <0.01; Student's t test.

Representative confocal images of mitochondrial morphology in raptor WT and KO, or rictor WT and KO MEFs are shown in Figures S3A-B.

(D-E) Levels of proteins relevant to mitochondrial fission and fusion and mTORC1 signaling in raptor WT and KO MEFs (D), or rictor WT and KO MEFs (E). α-tubulin and β-actin were used as loading controls. Quantification of levels of the indicated proteins is shown in Figure S3C.

See also Figure S3.

Figure 4. mTORC1 activation by TSC2 deletion induces mitochondrial fragmentation.

(A) Levels of the indicated proteins in TSC2 wild-type (WT) and knockout (KO) MEFs. α-tubulin was used as a loading control. Quantification of levels of the indicated proteins is shown in Figure S3D.

(B) Representative confocal images of mitochondrial morphology in TSC2 WT and KO MEFs. Mitochondria were labeled using an anti-TOM20 antibody. ** indicates cells with fragmented mitochondria. Scale bars represent 20 μm.

(C) Quantification of mitochondrial morphology in TSC2 WT and KO cells. n = 191 for TSC2 WT, n = 226 for TSC2 KO from three independent experiments. Data represent mean ± SD. *P < 0.05, **P <0.01; Student's t test.

See also Figure S3.

Figure 5. 4E-BPs mediate mTORC1-dependent mitochondrial fission.

(A-B) Representative TEM images of 4E-BP1/2 double knockout (4E-BP DKO) MEFs treated with vehicle (A) or Ink1341 (200 nM) (B) for 24 hr showing mitochondria (Mito), endoplasmic reticulum (ER) and autophagosomes (AP). Scale bars represent 1 μm. Representative TEM images of 4E-BP1/2 wild-type (4E-BP WT) MEFs treated with vehicle or Ink1341 are shown in Figures S4A-B.

(C-F) Quantification of TEM images of 4E-BP WT and 4E-BP DKO MEFs treated with vehicle or Ink1341 (200 nM) showing mitochondrial length (C), percentage of branched mitochondria (D), mitochondrial area per cytoplasmic area (E) and autophagosome area per cytoplasmic area (F). Data are shown as 0 to 100% box plots with the 25th, 50th, and 75th percentiles as the lower, middle, and upper boundaries of the box, respectively. For (C-D), n = 810 for WT + vehicle, n = 504 for WT + Ink1341, n = 691 for DKO + vehicle, n = 719 for DKO + Ink1341 from three independent experiments. For (E-F), n = 30 cells per group from three independent experiments. $*P < 0.05$, $**P < 0.01$, $***P < 0.001$; two-way ANOVA with Tukey's post-hoc test.

(G) Quantification of mitochondrial morphology by confocal microscopy in 4E-BP WT and DKO MEFs treated with vehicle or Ink1341 (200 nM) (top). Mitochondria were labelled with an anti-TOM20 antibody. Data represent mean ± SD. n = 333 for WT + vehicle; n = 261 for WT + Ink1341; n = 315 for DKO + vehicle; n = 333 for DKO + Ink1341 from three independent experiments. $***P < 0.001$; Student's t test. Representative confocal images of cells with the indicated mitochondria (bottom).

(H) Representative images of mitochondrial morphology and DRP1 localization in 4E-BP1/2 DKO MEFs treated with vehicle (left) or Ink1341 (right). Mitochondria and DRP1 were stained with anti-TOM20 and anti-DRP1 antibodies, respectively. Scale bars represent 10 μm.

See also Figures S5 and S6.

Figure 6. Translational control of MTFP1 by the mTORC1/4E-BP signaling pathway.

(A) Polysome profiles of 4E-BP1/2 wild-type (4E-BP WT) MEFs treated with vehicle or Ink1341 (200 nM) for 12 hr. Absorbance at 254 nm was recorded continuously. 40S, 60S and 80S denote the positions of corresponding ribosomal subunits and monosomes.

(B) Distribution of *Mtfp1*, *CyclinD3* and β-*actin* mRNAs in polysome profiles from (A) was determined by RT-qPCR. Data represent mean ± SD. A representative experiment of two independent experiments (each carried out in triplicate) is presented.

(C) Polysome profiles of 4E-BP1/2 double knockout (4E-BP DKO) MEFs treated with vehicle or Ink1341 (200 nM) for 12 hr. Absorbance at 254 nm was recorded continuously. 40S, 60S and 80S denote the positions of corresponding ribosomal subunits and monosomes.

(D) Distribution of *Mtfp1*, *CyclinD3* and β-*actin* mRNAs in polysome profiles from (C) was determined by RT-qPCR. Data represent mean ± SD. A representative experiment of two independent experiments (each carried out in triplicate) is presented.

(E) Levels of proteins relevant to mitochondrial fission, mTORC1 signaling and autophagy in 4E-BP WT and DKO MEFs treated with vehicle or Ink1341 for 24 hr. α-tubulin was used as a loading control. Quantification of levels of the indicated proteins is shown in Figure S4G.

See also Figures S5 and S6.

Figure 7. Translational regulation of mitochondrial fission and cell survival by the mTORC1/4E-BP/MTFP1 signaling axis.

(A) Levels of proteins relevant to mitochondrial fission and mTORC1 signaling in empty vector (control) and MTFP1-overexpressing (MTFP1) MEFs treated with vehicle or Ink1341 (200 nM) for 24 hr. α-tubulin was used as a loading control. Quantification of levels of the indicated proteins is shown in Figure S8A.

(B) Representative confocal images of mitochondrial morphology in control and MTFP1-overexpressing MEFs treated with vehicle or Ink1341 (200 nM) for 24 hr. Mitochondria were labeled using an anti-TOM20 antibody. Scale bars represent 20 μm. * and ** indicate cells with elongated and fragmented mitochondria, respectively.

(C) Quantification of mitochondrial morphology in control and MTFP1-overexpressing MEFs treated with vehicle or Ink1341 (200 nM) for 24 hr. n = 179 for control + vehicle, n = 115 for control + Ink1341, n = 213 for MTFP1 + vehicle, n = 173 for MTFP1 + Ink1341 from three independent experiments. Data represent mean ± SD. **P <0.01, ***P < 0.001; Student's t test.

(D-E) Cell proliferation was assayed by 5-bromo-2'-deoxyuridine (BrdU) incorporation (D) or Giemsa staining (E). BrdU incorporation was measured in control and MTFP1-overexpressing MEFs treated with vehicle, Ink1341 (200 nM) or Ink128 (200 nM) for 48 hr (D). Data represent mean ± SEM. A representative experiment of three independent experiments (each carried out in n = 5) is presented. Control and MTFP1-overexpressing MEFs were treated with the indicate drug and visualized with Giemsa staining (E). *P < 0.05; two-way ANOVA with Tukey's post-hoc test.

(F) Caspase-3/7 activity in cells (D-E) was measured by a fluorometric caspase-3/7 activity assay. Data represent mean ± SEM. A representative experiment of two independent experiments (each carried out in n = 6) is presented. ***P < 0.001; two-way ANOVA with Tukey's post-hoc test.

See also Figures S6 and S7.

CONTACT FOR REAGENT AND RESOURCE SHARING

Further information and requests for reagents may be directed to the Lead Contact, Nahum Sonenberg (nahum.sonenberg@mcgill.ca)

EXPERIMENTAL MODEL AND SUBJECT DETAILS

Cell Lines and Cell Culture Conditions

Cells were maintained in DMEM containing 10% FBS and 100 units/ml penicillin/streptomycin (all from Invitrogen) at 37°C and 5% CO_2. WT ($p53^{-/-}$) and 4E-BP DKO ($p53^{-/-}$) MEFs were described (Petroulakis et al., 2009). Inducible raptor and rictor KO MEFs were described (Cybulski et al., 2012; Robitaille et al., 2013). TSC2 WT ($p53^{-/-}$) and KO ($p53^{-/-}$) MEFs were described (Zhang et al., 2003). A375 cells were obtained from ATCC (CRL-1619). Cells were seeded at ~20% confluency, grown overnight and treated with vehicle (DMSO), Ink1341 (200 nM), Ink128 (200nM), Torin1 (200 nM), rapamycin (200 nM) and PMA (100 nM) for 24 hr or the indicated time.

METHOD DETAILS

Transmission Electron Microscopy

MEFs (70% confluency) treated with vehicle (DMSO), Ink1341 (200 nM) or rapamycin (200 nM) for 24 hr were washed with PBS 3 times each for 1 minute (min) and fixed with 100 mM sodium cacodylate buffer containing 2.5% glutaraldehyde (pH 7.4) for 2 hr at 4°C. Samples were washed 3 times each for 1 min with sodium cacodylate buffer containing 5% sucrose (pH 7.4) at 4°C, followed by osmification with 2% OsO_4 in sodium cacodylate buffer containing 3% potassium ferrocyanide and 5% sucrose for 2 hr at 4°C. This was followed by washing 3 times each for 1 min with sodium cacodylate buffer containing 5% sucrose (pH 7.4). Samples were then stained with sodium cacodylate buffer containing 1% tannic acid and 5% sucrose for 1 hr at 4°C.

The solution was replaced by sodium cacodylate buffer containing 1% sodium sulfate and 5% sucrose for 20 min at 4°C. This solution was further replaced by 100 mM sodium maleate (pH 5.7) for 10 min, followed by sodium maleate buffer containing 6% uranyl acetate (pH 5.7) for 2 hr at 4°C. Samples were washed with sodium maleate buffer (pH 5.7) 3 times each for 1 min. Samples were dehydrated through graded alcohols (50%-100%) at room temperature (RT), followed by embedding in epoxy resin diluted 1:1 with 100% alcohol for 1 hr and 100% epoxy for 1 hr, followed by 2 hr in a desiccated vacuum container and overnight polymerization at 65°C. Blocks were trimmed and cut at 90 to 100 nm thick with an UltraCut E ultramicrotome (Reichert-Jung). Serial sections were transferred onto a 200-mesh Cu grid, and poststained with 4% uranyl acetate for 8 min and then with Reynold's lead for 5 min. Cells on the grids were observed with a transmission EM (FEI Tecnai 12; FEI) operated at 120 kV, and images were collected with a CCD camera (AMT XR 80 C). For quantification analysis, low-magnification EM images of the cells were taken. On these images, all mitochondria, ER and autophagosomes were identified manually using Adobe Photoshop software. The length and area of each mitochondrion and autophagosome, as well as the total cytoplasmic area of each cell, were measured (Photoshop software). Data are shown as 0 to 100% box plots with the 25th, 50th, and 75th percentiles as the lower, middle, and upper boundaries of the box, respectively, from three independent experiments.

Focused Ion Beam-Scanning Electron Microscope

Sample blocks for 3-D characterization by FIB-SEM were prepared as described above for TEM. Each trimmed Epon block was mounted on a 45° pre-titled SEM stub and coated with a 2 nm platinum layer to enhance electrical conductivity. Milling of serial sections and imaging of block face after each z-slice was carried out with the FEI Helios Nanolab 660 DualBeam (FEI Co., Hillsboro, OR USA) using the FEI Auto Slice & View G3 ver 1.4 software (http://www.fei.com/software/auto-slice-and-view).

A block was first imaged to determine the orientation relationship between the block face and ion and electron beams. In the experiments, theta (Ө), the angle between the block face and the 45° pre-titled SEM stub, was found to be -13°. A protective carbon layer 20-μm long, 5-μm wide and 2-μm thick was deposited on the surface of the region that contained cells without bias to protect the resin volume and correct for stage and/or specimen drift, i.e. perpendicular to the image face of the volume to be milled. Trenches on either side of the region were created to minimize re-deposition during the automated milling and imaging. Imaging fiducial was generated for both ion beam and electron beam imaging and used to dynamically correct for specimen and stage drift. Milling was performed at 30 kV with an ion beam current of 0.79 nA, stage tilt of -6°, working distance of 4 mm, and increments of 4 nm in the Z-direction. Each newly milled block face was imaged with the solid-state, high energy in-column detector (ICD) for backscattered electrons at an accelerating voltage of 2 kV, beam current of 0.4 nA, stage tilt of 32°, and working distance of 2.5 mm. The pixel resolution was 3.4 nm (X-direction) by 3.4 nm (Y-direction) with a dwell time of 30 μs. Pixel dimensions of the recorded image were 3072 x 2048 pixels. One hundred and eighty images were collected for each block and the contrast of the images inversed. Visualization and direct 3-D volume rendering of the acquired datasets was performed with Amira 6.0.1 software (http://www.fei.com/software/amira-3d-for-life-sciences; FEI Co., Hillsboro, OR USA) with 30 successive images selected based on the region of interest, i.e., mitochondria.

Immunofluorescence

Immunofluorescence were performed as previously described (Prudent et al., 2015). Briefly, cells were fixed in 5 % paraformaldehyde (PFA) (Sigma) in PBS at 37°C for 15 min, then washed 3 times with PBS, followed by quenching with 50 mM ammonium chloride in PBS. After 3 washes in PBS, cells were permeabilized in 0.1 % Triton X-100 (Sigma) in PBS, followed by 3 washes in PBS. Then cells were blocked with 10 % fetal bovine serum (FBS) in PBS, followed by

incubation with primary antibodies in 5 % FBS in PBS, for 1 hr at RT. After 3 washes with 5 % FBS in PBS, cells were incubated with Alexa fluor 488, 594 or 647, secondary antibodies (1:1000) (Invitrogen) for 1 hr at RT. After 3 washes in PBS, coverslips were mounted onto slides using Dako fluorescence mounting medium (Dako).

Stained cells were imaged using a 60X or a 100X objective lenses (NA1.4) on an Olympus IX81 inverted microscope with appropriate lasers using an Andor/Yokogawa spinning disk system (CSU-X), with a sCMOS camera, coupled with the MetaMorph software. For mitochondrial morphology analysis, 1-3 stacks of 0.2-0.4 μm each were acquired using the 60X objective. Images were then compiled by "max projection" and mitochondrial morphology was analyzed and presented as intermediate, elongated or fragmented. For DRP1 analysis, a 0.2 μm z axis image series (5-7 stacks) of cells labelled for TOM20 and DRP1 were obtained using the 100X objective and stacked in the same condition of gain, laser intensities and exposure time. Images were then compiled as "Max projection" and analyzed using the FIJI software.

mTOR inhibitors, lentivirus infection, siRNA and GFP-DRP1 plasmid transfection

Ink1341 and Ink128 were provided by Intellikine. Torin1 and rapamycin were purchased from Tocris Bioscience. PMA was purchased from EMD Millipore Corporation.

For lentivirus production, lentiviral vectors were co-transfected into HEK293T cells with the lentivirus packaging plasmids PLP1, PLP2 and PLP-VSVG (Invitrogen) using Lipofectamine 2000 (Invitrogen). Supernatants were collected 48 hr post infection, passed through a 0.45 μm nitrocellulose filter, and applied on target cells with polybrene (1 μg/ml). Cells were selected with puromycin (5 μg/ml) for 48 hr. Lentiviral vectors encoding MTFP1 (EX-T9261-Lv105 and EX-T9261-Lv151) cDNAs were obtained from GeneCopoeia.

For small interference (si) RNA experiments, cells were transfected using Lipofectamine RNAimax (Invitrogen) with 20 nM siRNA for 3 days. A control siRNA (Silencer Selected

Negative Control siRNA, Invitrogen) was used for each experiment. To silence MTFP1, TSC2 WT and KO cells were transfected with siRNA against MTFP1 (Silencer Selected Pre-Designed siRNA against MTFP1 s85882, Invitrogen). For transient transfection of GFP-DRP1 plasmids, MEFs were transfected using Lipofectamine 3000 reagent (Invitrogen) according to the manufacturer's recommendations.

CRISPR-mediated gene knockout

A375 cells were transfected in 6 well plates with a plasmid expressing hCas9 (Addgene plasmid #41815) (0.7 μg); gRNA targeting 4E-BP1 (purchased from GeneCopoeia, cat. # HCP204676-SG01-3-B-a; HCP204676-SG01-3-B-b; and HCP204676-SG01-3-B-c against 4E-BP1 sequences CCGCCCGCCCGCTTATCTTC; GTGAGTTCCGACACTCCATC; and TGAAGAGTCACAGTTTGAGA, respectively); gRNA targeting 4E-BP2 (purchased from GeneCopoeia, cat. # HCP254214-SG01-3-B-a; HCP254214-SG01-3-B-b; and HCP254214-SG01-3-B-c against 4E-BP2 sequences GTGGCCGCTGCCGGCTGACG; CTAGTGACTCCTGGGATATT; and ACAACTTGAACAATCACGAC) (0.2 μg for each gRNA to total 1.2 μg); and pBabe-puro (0.6 μg), using Lipofectamine 2000 (Invitrogen), according to the manufacturer's instructions. A plasmid expressing hCas9 was gifted from George Church (Addgene plasmid #41815) (Mali et al., 2013). As a control, cells were transfected with a plasmid expressing hCas9 (0.7 μg) and pBabe-puro (0.6 μg), using Lipofectamine 2000 (Invitrogen). Two days post-transfection, cells were selected for 3 days with puromycin (4 μg/ml) to remove non-transfected cells. Following selection, cells were seeded in 96 well plates at a density of single cell/well in puromycin free media. Cells were monitored to the presence of single colonies/well. Single cell colonies were amplified to generate cell lines and the expression of 4E-BP1 and 4E-BP2 was analysed by western blot. Lines with loss of 4E-BP1 and 4E-BP2 expression were kept

for further experiments. For the control cells, single cell colonies were amplified and 5 of the control lines were pooled to generate the A375 CRISPR control population.

BrdU incorporation, Giemsa staining, caspase-3/7 activity assay

Empty vector (control) and MTFP1-expressing cells (5×10^3) were seeded in a 96-well plate and treated with the indicated drugs in the figure legend. Cell proliferation rate was determined using Cell Proliferation Elisa BrdU kit (Roche). Absorbance at 370 nm (reference wavelength 492 nm) was measured using a Varioskan microplate reader (Thermo Fisher Scientific). Empty vector (control) and MTFP1-expressing cells (1.5×10^5) were seeded in a 6-well plate, treated with the indicated drugs for 48 hr and visualized with Giemsa staining. Caspase-3/7 activity was determined using Caspase Glo 3/7 Assay (Promega). Luminescence was measured using GloMax 96 Microplate Luminometer (Promega).

Cell lysis, Western blotting, antibodies

Cells were lysed in lysis buffer (50 mM Tris-HCl (pH 7.5), 150 mM NaCl, 1 mM EDTA, 1% NP-40, Roche complete protease inhibitor cocktail). Protein concentrations were determined with the Bio-Rad protein assay (Bio-Rad). Proteins were resolved by SDS-PAGE, and then transferred to PVDF membranes. Antibodies against phospho-DRP1 (S616) (#3455), phospho-DRP1 (S637) (#4867), 4E-BP1 (#9644), phospho-4E-BP1 (T37/46) (#2855), phospho-4E-BP1 (S65) (#9456), phospho-S6K (T389) (#9234), mTOR (#2983), ATG5 (#8540), LC3 (#4599), PARP (#9532), MFN1 (#14739) and α-tubulin (#2144) were from Cell Signaling Technology. Antibodies against MFN2 (sc-100560), S6K1 (sc-230), TOM20 (sc-11415) and TSC2 (sc-893) were from Santa Cruz Biotechnology Inc. Antibodies against DRP1 (611113) and OPA1 (612606) were from BD Biosciences. MTFP1 (ab198217), rictor (A300-459), raptor (09-217) and β-actin (A5441) were from Abcam, Bethyl Laboratories Inc., EMD Millipore Corporation and Sigma-

Aldrich Co., respectively. Horseradish peroxidase-conjugated anti-rabbit IgG and anti-mouse IgG were from Amersham Biosciences (Baie d'Urfé). For immunofluorescence, goat anti-mouse and goat anti-rabbit Alexa Fluor 488, 597 or 647 were used as secondary antibodies (Invitrogen).

Polysome profiling, RNA isolation, RT-qPCR

Polysome profiling and RT-qPCR were carried out as described previously (Gandin et al., 2014). Briefly, cells were cultured in 15-cm dishes, treated with vehicle or Ink1341 (200 nM) for 12 hr, incubated in growth media containing 100 μg/ml cycloheximide for 5 min at 37°C, washed twice with cold PBS containing 100 μg/ml cycloheximide, collected and lysed in 450 μl of hypotonic buffer (5 mM Tris-HCl (pH 7.5), 2.5 mM $MgCl_2$, 1.5 mM KCl, 100 μg/ml cycloheximide, 2 mM DTT, 0.5% Triton X-100 and 0.5% sodium deoxycholate). Lysates were loaded onto 10-50% (wt/vol) sucrose density gradients (20 mM HEPES-KOH (pH 7.6), 100 mM KCl and 5 mM $MgCl_2$) and centrifuged at 35,000 rpm (SW 40 Ti rotor, Beckman Coulter, Inc.) for 2 hr at 4°C. Gradients were fractionated, and optical density at 254 nm was continuously recorded using an ISCO fractionator (Teledyne ISCO). RNA from each fraction and input was isolated using Trizol (Invitrogen) and GlycoBlue (Invitrogen) according to the manufacturer's instructions. RT-qPCR reactions were carried out using SuperScript III First-Strand Synthesis System (Invitrogen) and iQ SYBR Green Supermix (Bio-Rad) according to the manufacturer's instructions. Following primers were used: *Mtfp1*-forward 5'-TAATCCACCCCATCGACAG-3' and *Mtfp1*-reverse 5'-TCCACTGACGGGTACAGCTT-3'. Primers for *cyclin D3* and *β-actin* mRNAs were previously described (Dowling et al., 2010).

QUANTIFICATION AND STATISTICAL ANALYSIS

Quantification of Immunoblottings

For all quantification of band intensities, ImageJ software was used (https://imagej.nih.gov/ij/index.html).

Statistical analysis

Data represent mean ± SD or SEM, or are shown as 0 to 100% box plots with the 25th, 50th, and 75th percentiles as the lower, middle, and upper boundaries of the box, respectively. Differences among groups were compared using two-way ANOVA followed by between-group comparison with Tukey's post-hoc test, or Student's t-test (two-tailed, unpaired) when there were only two groups. All statistical analyses were performed using IBM SPSS Statistics Version 22 software. The differences were considered significant when $*P < 0.05$, $**P < 0.01$ and $***P < 0.001$. Statistical results, along with tests used, were summarized in Table S1.

DATA AND SOFTWARE AVAILABILITY

The original, unprocessed data have been deposited to Mendeley Data and are available at http://dx.doi.org/10.17632/mjfjdvvw75.1.

KEY RESOURCES TABLE

REAGENT or RESOURCE	SOURCE	IDENTIFIER
Antibodies		
Rabbit polyclonal phospho-DRP1 (S616) antibody	Cell Signaling Technology	3455
Rabbit polyclonal phospho-DRP1 (S637) antibody	Cell Signaling Technology	4867
Mouse monoclonal DRP1 antibody	BD Biosciences Laboratories	611113
Rabbit monoclonal phospho-4E-BP1 (T37/46) (236B4) antibody	Cell Signaling Technology	2855
Rabbit monoclonal phospho-4E-BP1 (S65) (174A9) antibody	Cell Signaling Technology	9456
Rabbit monoclonal 4E-BP1 (53H11) antibody	Cell Signaling Technology	9644
Rabbit polyclonal 4E-BP2 antibody	Cell Signaling Technology	2845
Rabbit monoclonal phospho-S6K (T389) antibody	Cell Signaling Technology	9234
Rabbit polyclonal S6K1 antibody	Santa Cruz Biotechnology	sc-230
Rabbit monoclonal phospho-S6 Ribosomal Protein (Ser240/244) (D68F8) antibody	Cell Signaling Technology	5364
Mouse monoclonal S6 ribosomal protein antibody	Santa Cruz Biotechnology	sc-74459
Rabbit monoclonal mTOR (7C10) antibody	Cell Signaling Technology	2983
Rabbit monoclonal phospho-eIF4E (S209) antibody	Abcam	ab76256
Mouse monoclonal eIF4E antibody	BD Biosciences	610270
Rabbit polyclonal MTFP1 antibody	Abcam	ab198217
Rabbit monoclonal MFN1 (D6E2S) antibody	Cell Signaling Technology	14739
Rabbit polyclonal MFF antibody	Cell Signaling Technology	86668
Rabbit monoclonal ATG5 (D5F5U) antibody	Cell Signaling Technology	12994
Rabbit monoclonal LC3A (D50G8) antibody	Cell Signaling Technology	4599
Rabbit monoclonal PARP (46D11) antibody	Cell Signaling Technology	9532
Rabbit polyclonal α-tubulin antibody	Cell Signaling Technology	2144
Mouse monoclonal MFN2 (XX-1) antibody	Santa Cruz Biotechnology Inc.	sc-100560
Rabbit polyclonal TOM20 (FL-145) antibody	Santa Cruz Biotechnology Inc.	sc-11415
Rabbit polyclonal TSC2 (C-20) antibody	Santa Cruz Biotechnology Inc.	sc-893
Mouse monoclonal OPA1 antibody	BD Biosciences	612606
Rabbit polyclonal rictor antibody	Bethyl Laboratories Inc.	A300-459
Rabbit polyclonal raptor antibody	EMD Millipore Corporation	09-217
Mouse monoclonal β-actin antibody	Sigma-Aldrich Co.	A5441
Rabbit polyclonal GFP antibody	MBL Co.	598
Anti-rabbit IgG, horseradish peroxidase (HRP)-linked Antibody	Cell Signaling Technology	7074
Anti-mouse IgG, horseradish peroxidase (HRP)-linked Antibody	Cell Signaling Technology	7076
Goat anti-mouse IgG (H+L) secondary antibody, Alexa Fluor 488	Invitrogen	A-11029
F(ab')2-goat anti-rabbit IgG (H+L) secondary antibody, Alexa Fluor 488	Invitrogen	A-11070

Goat anti-mouse IgG (H+L) secondary antibody, Alexa Fluor 594	Invitrogen	A-11005
Goat anti-rabbit IgG (H+L) secondary antibody, Alexa Fluor 594	Invitrogen	A-11012
Goat anti-mouse IgG (H+L) secondary antibody, Alexa Fluor 647	Invitrogen	A-21235
Goat anti-rabbit IgG (H+L) secondary antibody, Alexa Fluor 647	Invitrogen	A-21244
Plasmids		
pCRISPR-SG01-3 (3 x sgRNA targeting 4E-BP1)	GeneCopoeia	HCP204676-SG01-3
pCRISPR-SG01-3 (3 x sgRNA targeting 4E-BP2)	GeneCopoeia	HCP254214-SG01-3
pCas9	Addgene (Mali et al., 2013)	41815
Lenti-Pac HIV Expression Packaging Kit	GeneCopoeia	LT001
pReceiver-Lv105-empty control	GeneCopoeia	EX-NEG-Lv105
pReceiver-Lv105-MTFP1	GeneCopoeia	EX-T9261-Lv105
pReceiver-Lv151-empty control	GeneCopoeia	EX-NEG-Lv151
pReceiver-Lv151-MTFP1	GeneCopoeia	EX-T9261-Lv151
pEGFP-N1-DRP1 WT	(Cribbs and Strack, 2007)	N/A
pEGFP-N1-DRP1 S616D	(Cribbs and Strack, 2007)	N/A
pEGFP-N1-DRP1 S637A	(Cribbs and Strack, 2007)	N/A
pEGFP-N1-DRP1 S616D/S637A	(Cribbs and Strack, 2007)	N/A
Chemicals		
Ink1341	Gifted from Intellikine	N/A
Ink128	Cayman chemical	11811
Torin1	Tocris Bioscience	4247
Rapamycin	Tocris Bioscience	1292
PMA	EMD Millipore Corporation	524400
Critical Commercial Assays		
Cell Proliferation Elisa BrdU (colorimetric)	Roche	11647229001
Caspase Glo 3/7 Assay Systems	Promega corporation	G8093
Deposited Data		
Raw image data	This paper	Mendeley data: http://dx.doi.org/10.17632/mjfjdvvw75.1
Experimental Models: Cell Lines		
WT (p53$^{-/-}$) and 4E-BP DKO (p53$^{-/-}$) MEFs	(Petroulakis et al., 2009)	N/A
Inducible raptor WT and KO MEFs	(Cybulski et al., 2012)	N/A
Inducible rictor WT and KO MEFs	(Cybulski et al., 2012)	N/A
TSC2 WT (p53$^{-/-}$) and KO (p53$^{-/-}$) MEFs	(Zhang et al., 2003)	N/A
A375 cells	ATCC	CRL-1619
WT (p53$^{-/-}$) MEFs expressing MTFP1	This paper	N/A
Inducible raptor KO MEFs expressing MTFP1	This paper	N/A
Oligonucleotides		
Silencer Select Negative Control No. 1 siRNA	Invitrogen	4390843
Silencer Select Pre-Designed siRNA against MTFP1 (siRNA ID: s85882)	Invitrogen	4390771
qPCR primer: Mtfp1 forward: TAATCCACCCCATCGACAG	This paper	N/A

qPCR primer: Mtfp1 reverse: TCCACTGACGGGTACAGCTT	This paper	N/A
qPCR primer: Cyclin D3 forward: CGAGCCTCCTACTTCCAGTG	(Dowling et al., 2010)	N/A
qPCR primer: Cyclin D3 reverse: CCGAGCCTCCTACTTCCAGTG	(Dowling et al., 2010)	N/A
qPCR primer: β-actin forward: GGCTGTATTCCCCTCCATCG	(Dowling et al., 2010)	N/A
qPCR primer: β-actin forward: CCAGTTGGTAACAATGCCATGT	(Dowling et al., 2010)	N/A
Software and Algorithms		
R	The R Project for Statistical Computing	N/A
ImageJ	NCBI	https://imagej.nih.gov /ij/index.html
IBM SPSS Statistics Version 22	IBM	N/A

Figure

Figure 1. Morita et al.
Active-site mTOR inhibitor induces mitochondrial elongation, branching and circularization
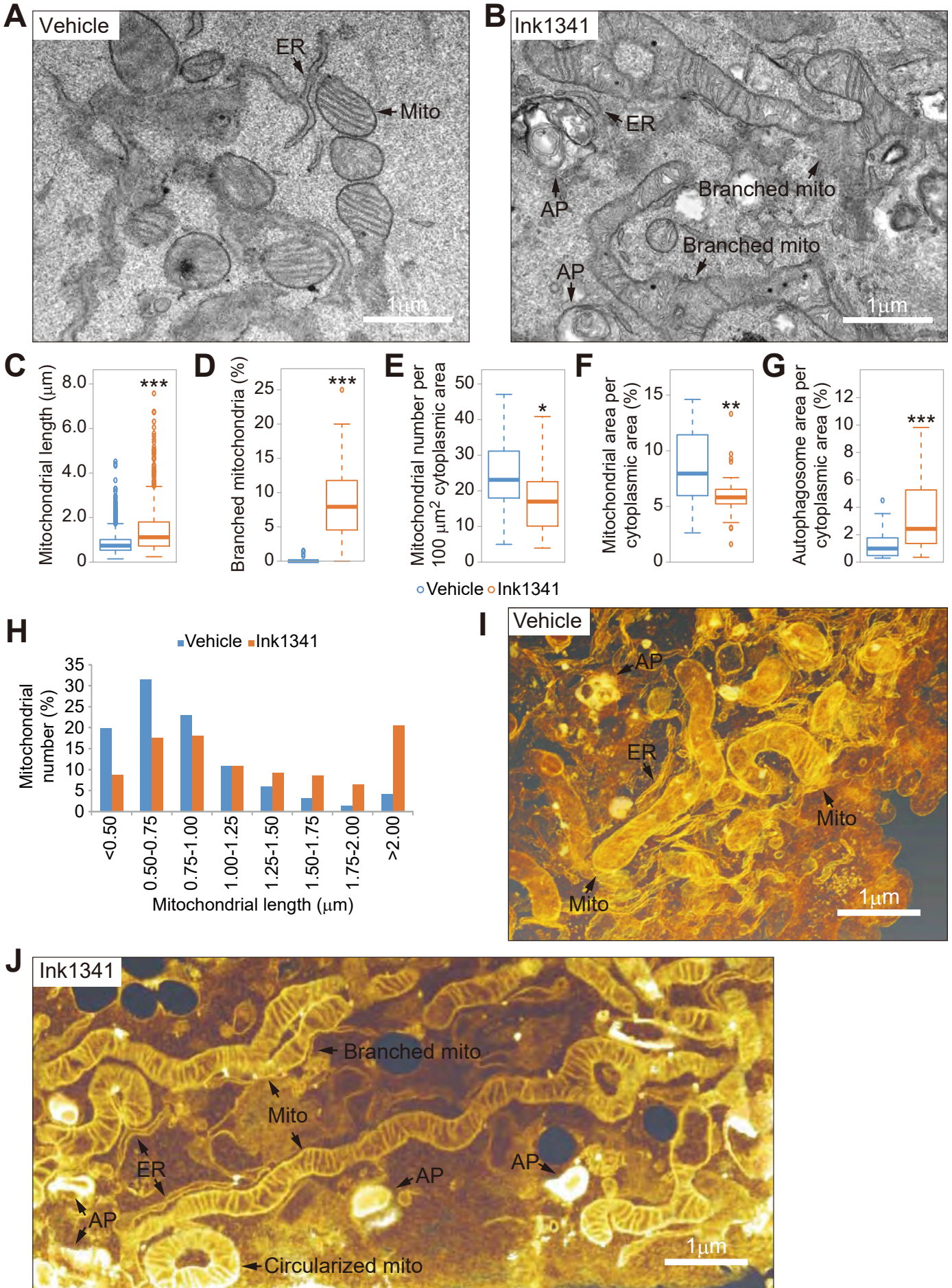
Figure 2. Morita et al.
Alterations in localization of DRP1 and protein levels of fission factors in asTORi-treated cells
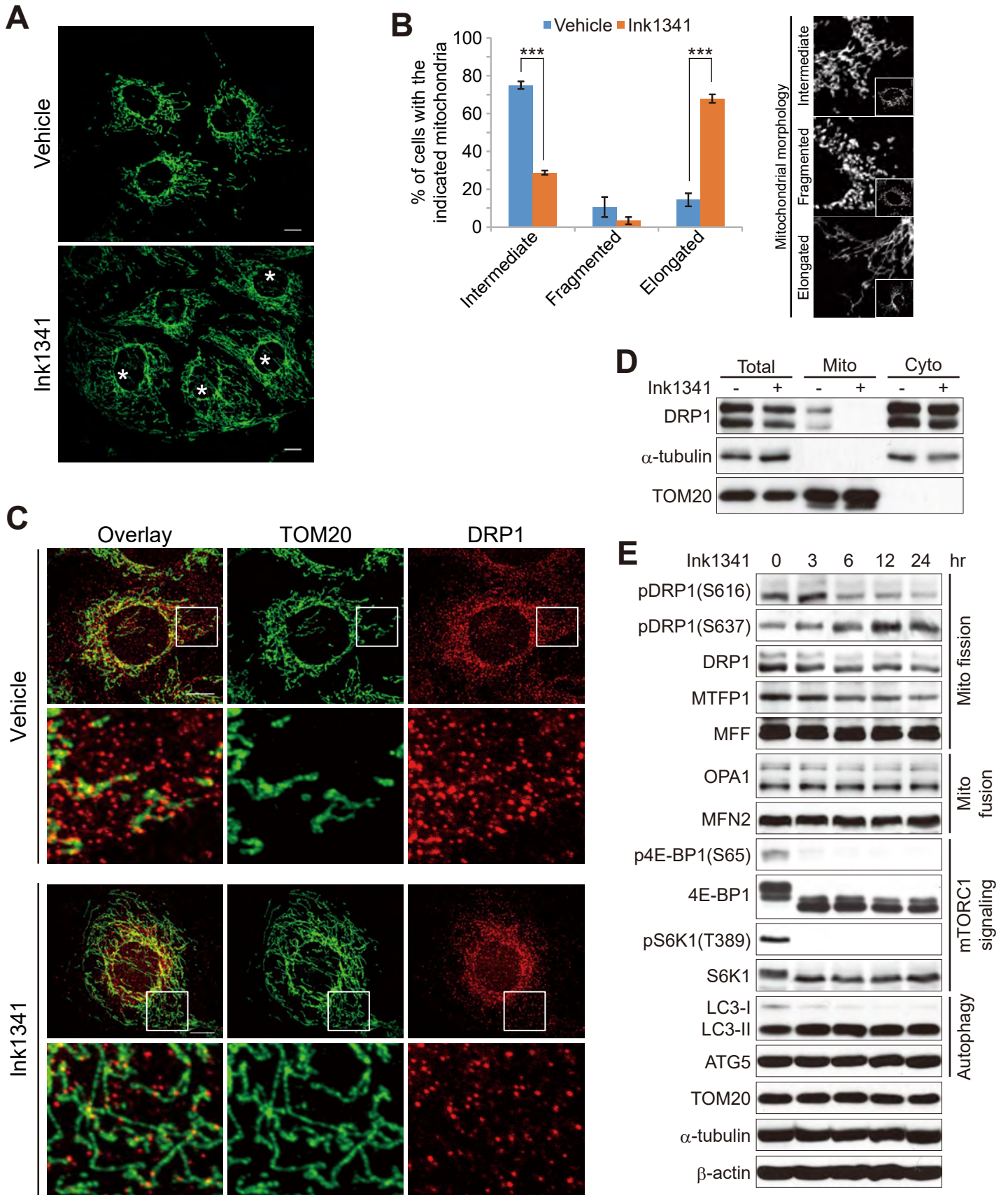
Figure 3. Morita et al.
mTORC1-dependent regulation of mitochondrial dynamics
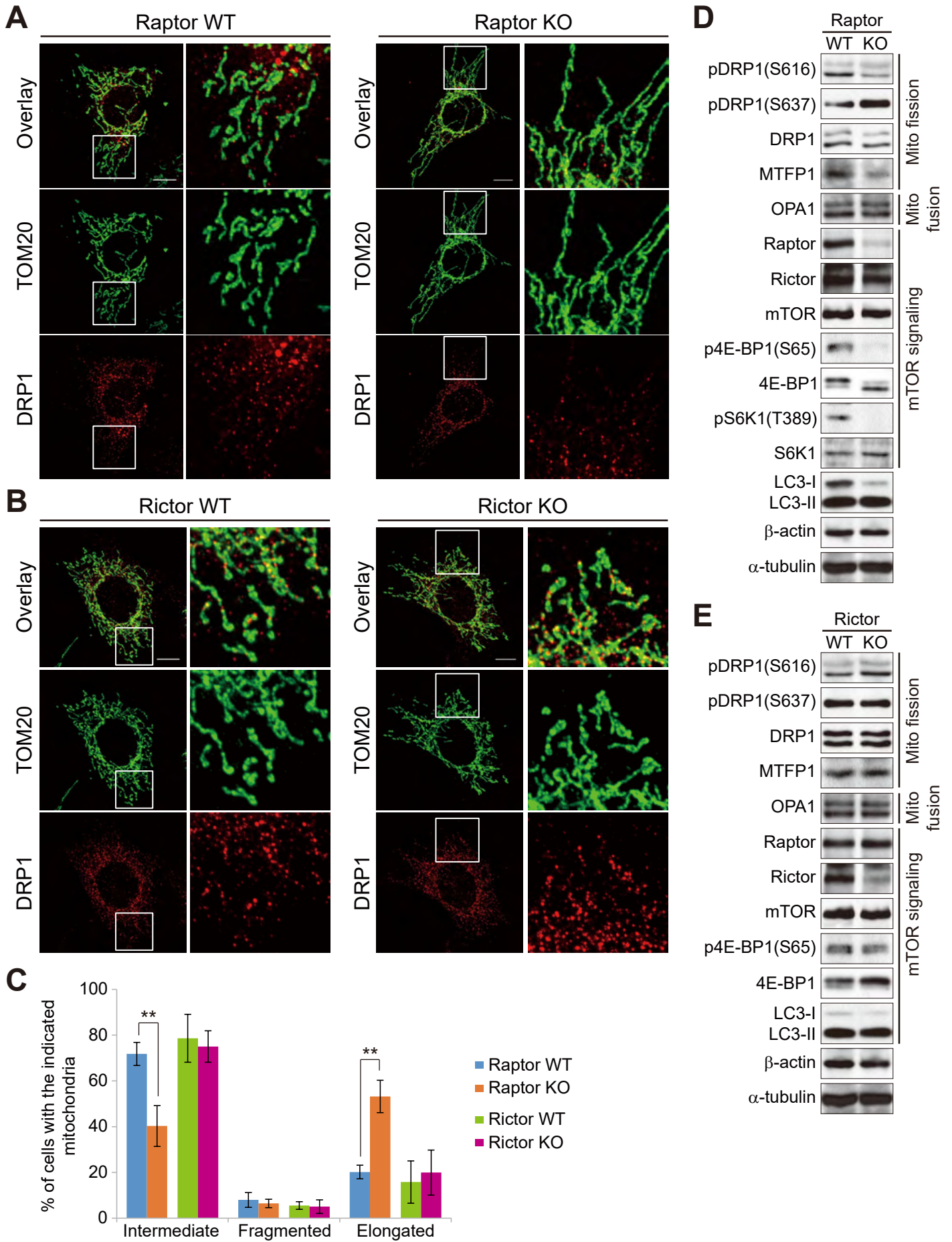
Figure 4. Morita et al.
mTORC1 activation by TSC2 deletion induces mitochondrial fragmentation
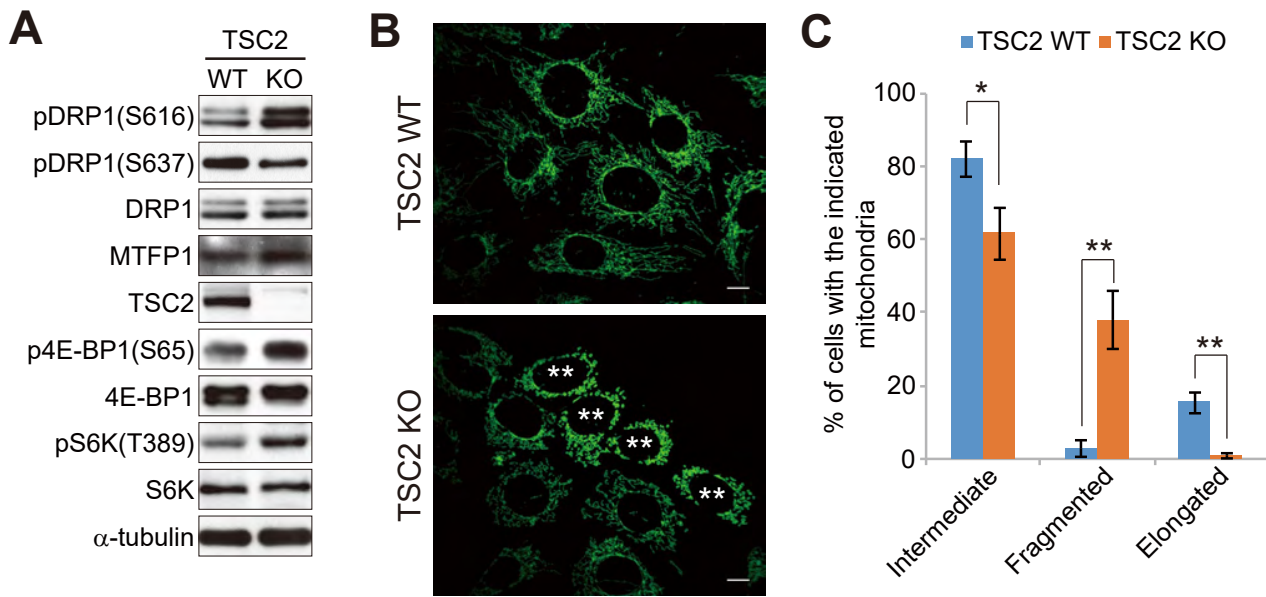
Figure 5. Morita et al.
4E-BPs mediate mTORC1-dependent mitochondrial fission
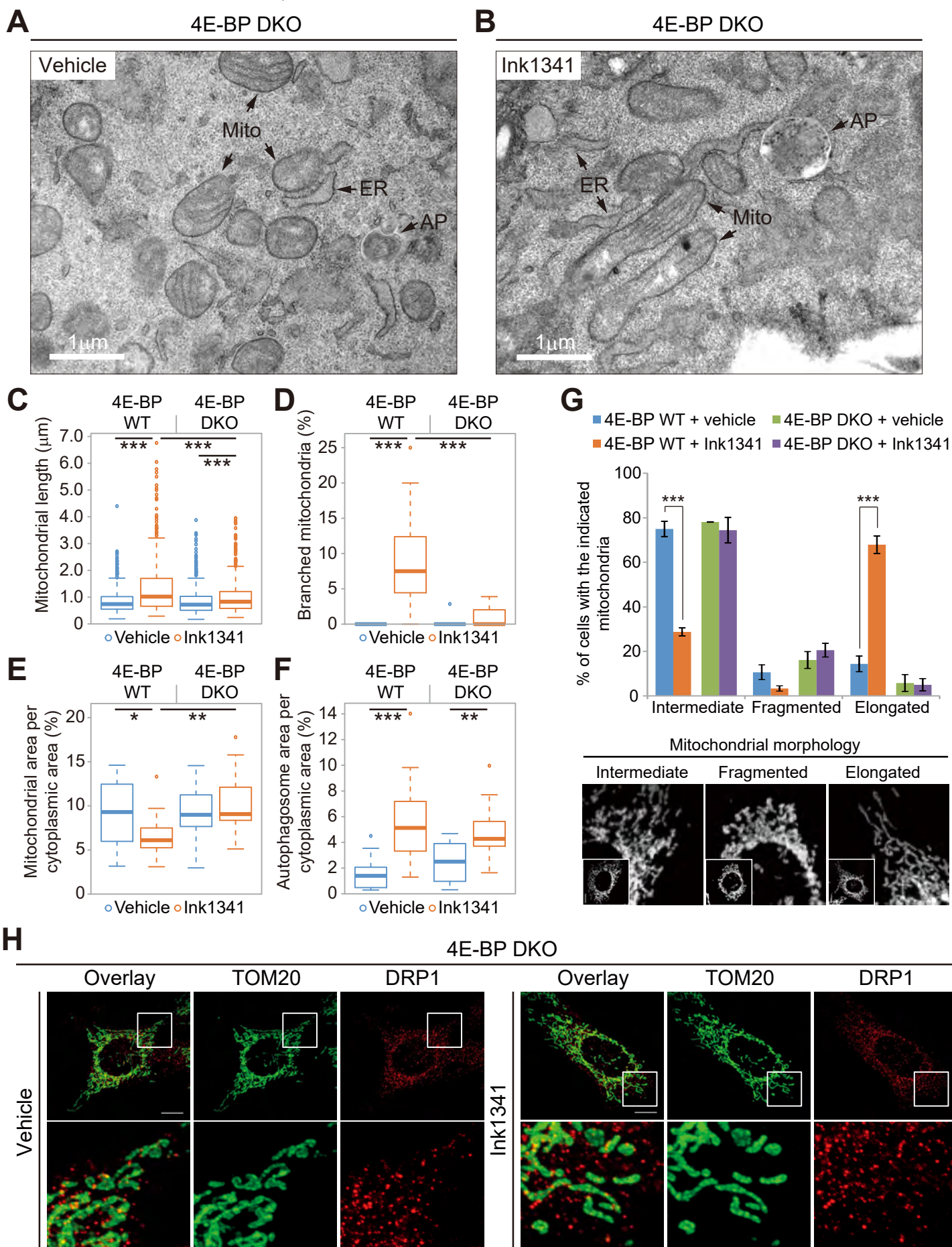
Figure 6. Morita et al.
Translational control of MTFP1 by the mTORC1/4E-BP signaling pathway
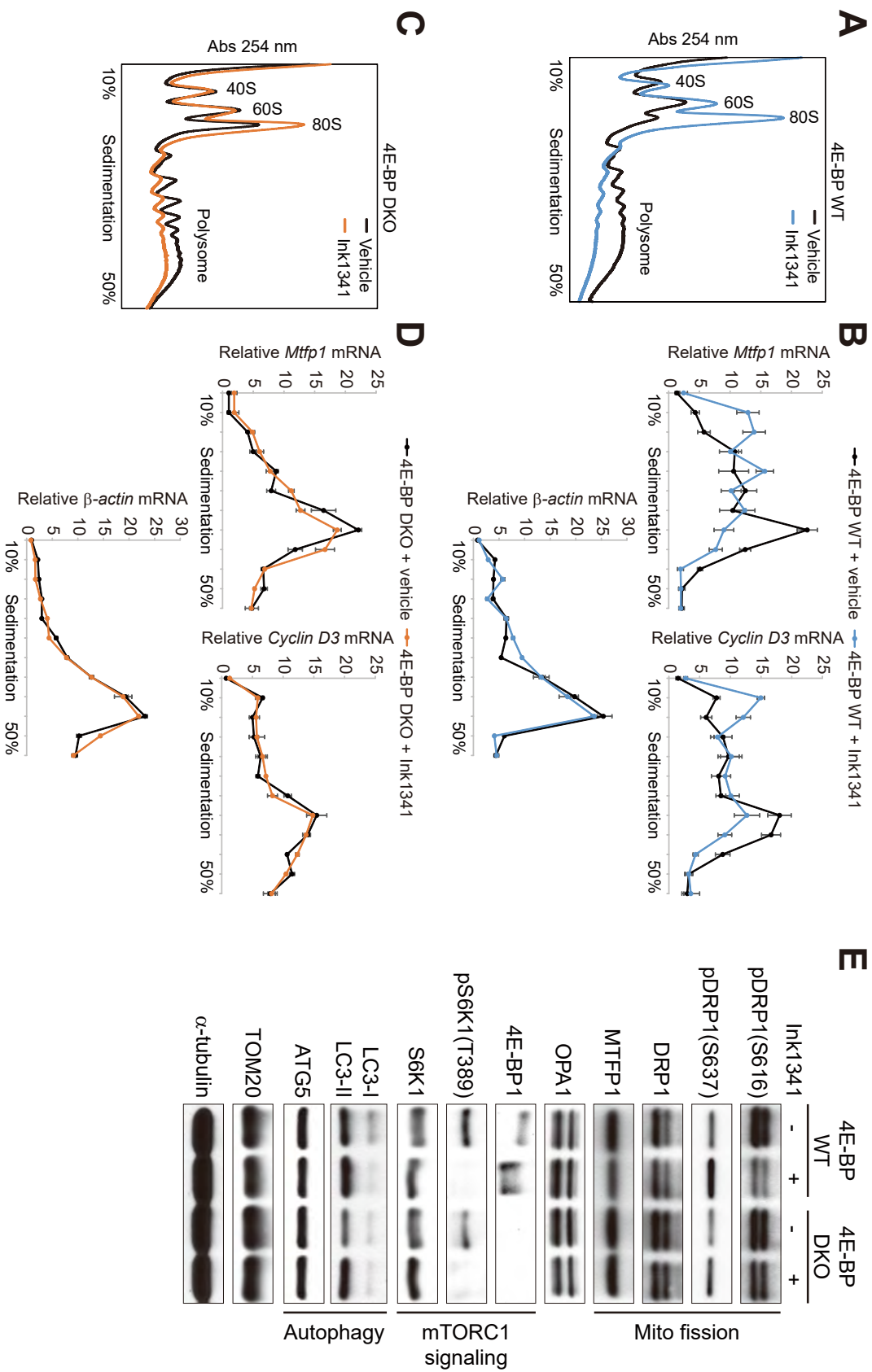
Figure 7. Morita et al.
Translational regulation of mitochondrial fission and cell survival by the mTORC1/4E-BP/MTFP1 signaling axis
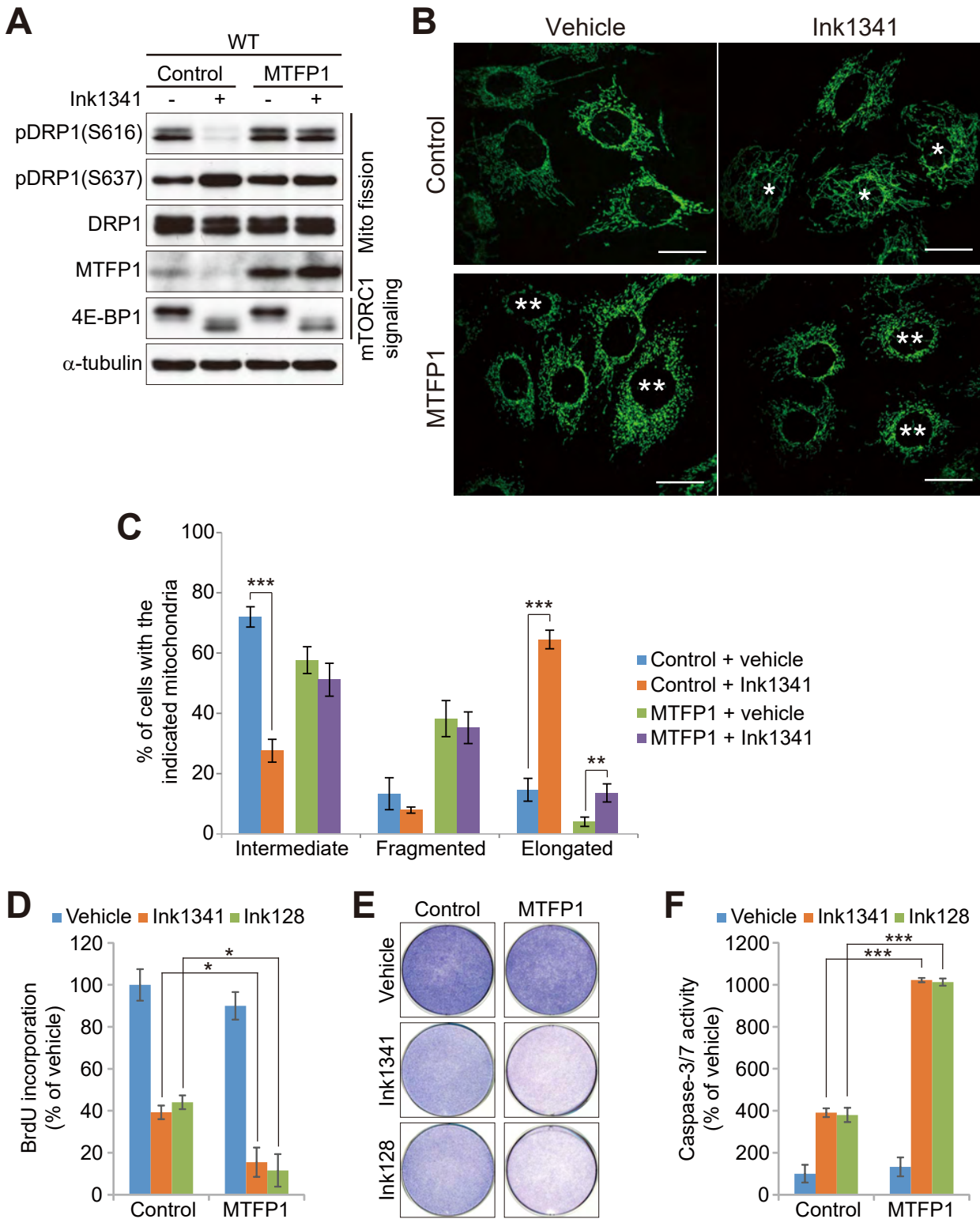
Supplemental Information

mTOR Controls Mitochondrial Dynamics and Cell Survival via MTFP1

Masahiro Morita*, Julien Prudent*, Kaustuv Basu, Vanessa Goyon, Sakie Katsumura, Laura Hulea, Dana Pearl, Nadeem Siddiqui, Stefan Strack, Shawn McGuirk, Julie St-Pierre, Ola Larsson, Ivan Topisirovic, Hojatollah Vali, Heidi M. McBride**, John JM Bergeron**, Nahum Sonenberg**

Figure S1, related to Figures 1 and 2.
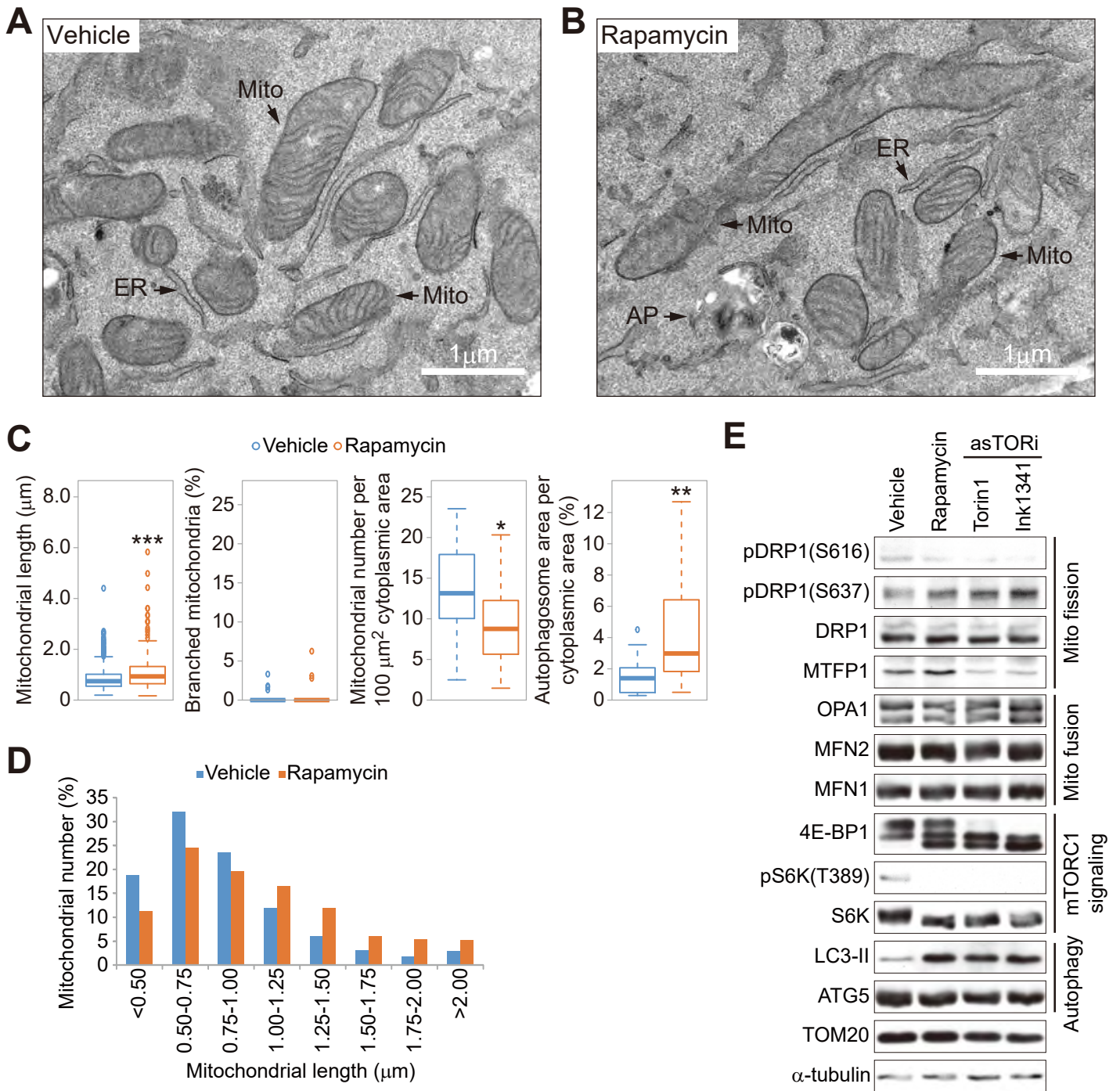
Figure S1, related to Figures 1 and 2. The effect of rapamycin on mitochondrial dynamics

(A-B) Representative transmission electron microscopy (TEM) images of wild-type (WT) MEFs treated with vehicle (DMSO) (A) or rapamycin (200 nM) (B) for 24 hr showing well-preserved mitochondria (Mito) and endoplasmic reticulum (ER) in (A), but elongated mitochondria, ER and autophagosomes (AP) in (B). Scale bars represent 1 μm.

(C-D) Quantification of TEM images of WT MEFs treated with vehicle or rapamycin (200 nM) for 24 hr showing mitochondrial length, percentage of branched mitochondria, mitochondrial number per 100 μm^2 of cytoplasmic area, autophagosome area per cytoplasmic area (C) and distribution of mitochondrial length (D). Data are shown as 0 to 100% box plots with the 25th, 50th, and 75th percentiles as the lower, middle, and upper boundaries of the box, respectively. For (C and D), n = 810 mitochondria for vehicle, n = 506 for rapamycin from three independent experiments. For mitochondrial number per 100 μm^2 of cytoplasmic area and autophagosome area per cytoplasmic area, n = 30 cells per group from three independent experiments. *$P < 0.05$, **$P < 0.01$, ***$P < 0.001$; Student's t test.

(E) Levels of proteins relevant to mitochondrial fission and fusion, mTORC1 signaling and autophagy in MEFs treated with vehicle, rapamycin (200 nM) and asTORis (200 nM) (Torin1 and Ink1341) for 24 hr. α-tubulin was used as a loading control.

Figure S2, related to Figures 1 and 2.
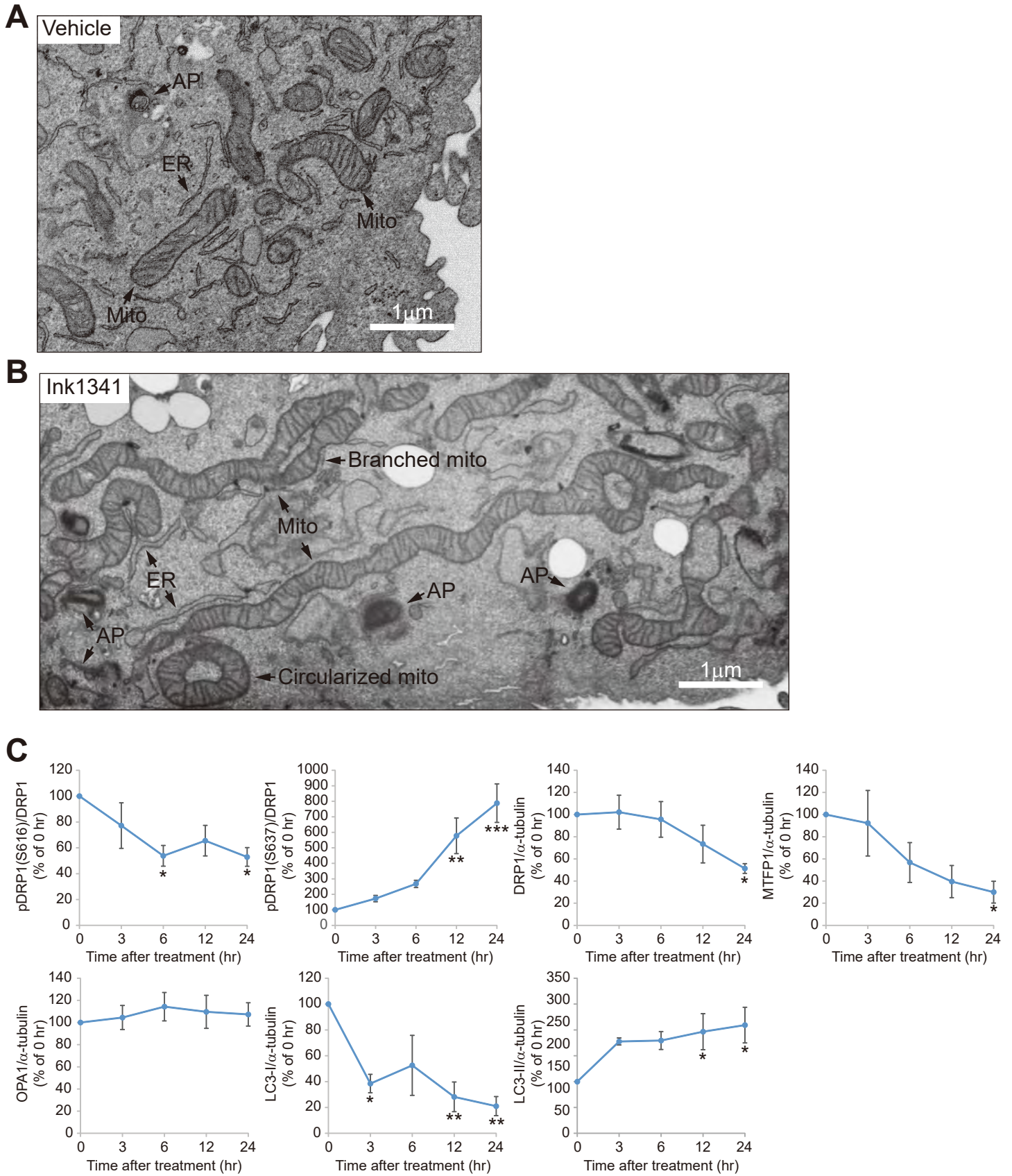
Figure S2, related to Figures 1 and 2. Active-site mTOR inhibitor induces mitochondrial elongation, branching and circularization

(A-B) Back scattered image of a single xy plane of one slice (4 nm thickness) obtained by FIB-SEM of WT MEFs treated with vehicle (A) and Ink1341 (200 nM) (B) for 24 hr showing well-preserved mitochondria (Mito), endoplasmic reticulum (ER) and autophagosomes (AP) in (A), but branched and circularized Mito, ER and AP in (B). Scale bars represent 1 μm.

(C) Quantification of levels of the indicated proteins in Figure 2E. Signal intensities were quantified by densitometry and normalized with a DRP1 or α-tubulin level. n = 4 per group. Data represent mean ± SEM. *P<0.05, **P<0.01, ***P< 0.001; one-way ANOVA with Tukey's post-hoc test.

Figure S3, related to Figure 3 and 4.
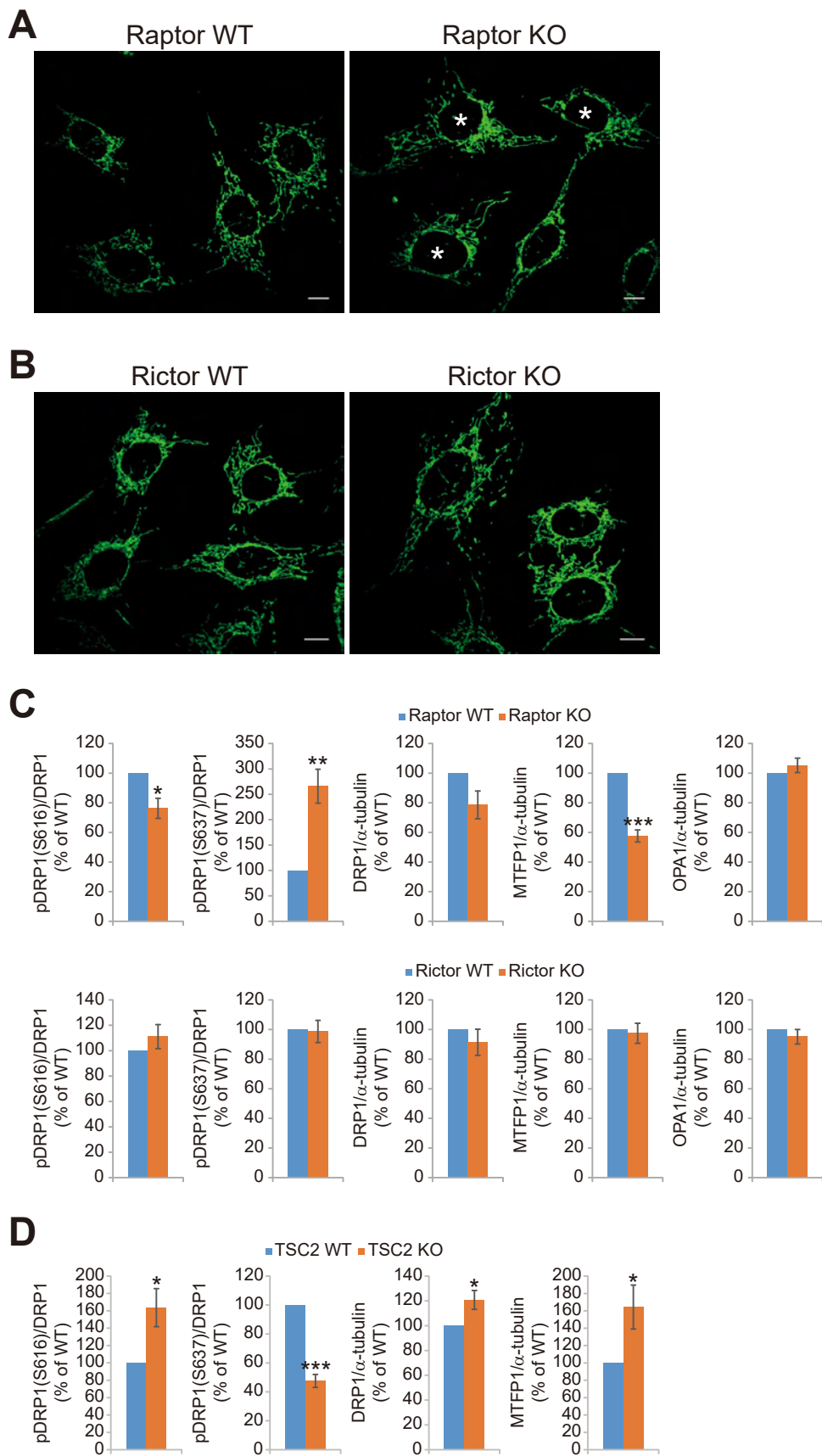
Figure S3, related to Figures 3 and 4. mTORC1-dependent regulation of mitochondrial dynamics

(A-B) Representative confocal images of mitochondrial morphology in raptor WT and knockout (KO) (A), or rictor WT and KO (B) MEFs. Mitochondria were labeled using an anti-TOM20 antibody. Scale bars represent 20 μm. * indicates cells with elongated mitochondria.

(C) Quantification of levels of the indicated proteins in Figures 3D-E. Signal intensities were quantified by densitometry and normalized with a DRP1 or α-tubulin level. n = 6 per group. Data represent mean ± SEM. *P<0.05, **P<0.01, ***P < 0.001; Student's t test.

(D) Quantification of levels of the indicated proteins in Figure 4A. Signal intensities were quantified by densitometry and normalized with a DRP1 or α-tubulin level. n = 4 per group. Data represent mean ± SEM. *P<0.05, ***P < 0.001; Student's t test.

Figure S4, related to Figures 5 and 6.
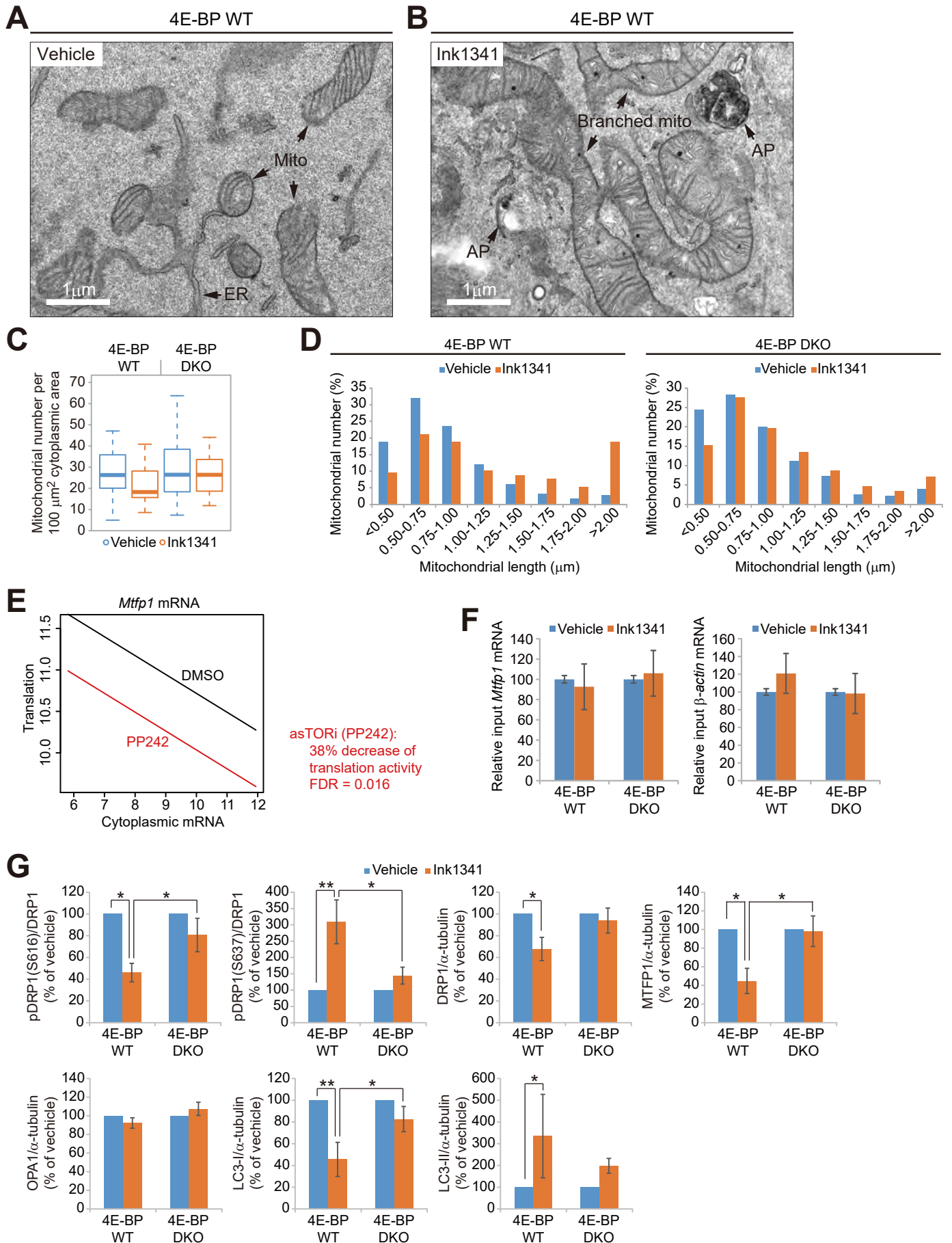
Figure S4, related to Figures 5 and 6. 4E-BPs mediate mTORC1-dependent regulation of mitochondrial dynamics and MTFP1 translation

(A-B) Representative TEM images of 4E-BP1/2 WT MEFs treated with vehicle (A) or Ink1341 (200 nM) (B) for 24 hr showing well-preserved mitochondria (Mito) and endoplasmic reticulum (ER) in (A), but elongated, branched and circularized mitochondria, ER and autophagosomes (AP) in (B). Scale bars represent 1 μm.

(C) Quantification of TEM images of 4E-BP1/2 WT and double knockout (4E-BP DKO) MEFs treated with vehicle or Ink1341 (200 nM) for 24 hr, showing mitochondrial number per 100 μm^2 of cytoplasmic area. n = 30 cells per group from three independent experiments. Data are shown as 0 to 100% box plots with the 25th, 50th, and 75th percentiles as the lower, middle, and upper boundaries of the box, respectively.

(D) Distribution of mitochondrial length in 4E-BP WT (left) and DKO (right) MEFs treated with vehicle or Ink1341 (200 nM) for 24 hr. n = 810 for WT + vehicle, n = 504 for WT + Ink1341, n = 691 for DKO + vehicle, n = 719 for DKO + Ink1341 from three independent experiments.

(E) The genome-wide translational analysis demonstrated repression of the translational activity of *Mtfp1* mRNA by asTORi (PP242) (1 μM) for 12 hr (Larsson et al., 2012).

(F) Relative input levels of *Mtfp1* and *β-actin* mRNAs in 4E-BP WT and DKO MEFs treated with vehicle or Ink1341 (200 nM) for 12 hr were quantified by RT-qPCR. Data represent mean ± SD. A representative experiment of two independent experiments (each carried out in triplicate) is presented.

(G) Quantification of levels of the indicated proteins in Figure 6E. Signal intensities were quantified by densitometry and normalized with a DRP1 or α-tubulin level. n = 4 per group. Data represent mean ± SEM. *P <0.05, **P <0.01; two-way ANOVA with Tukey's post-hoc test.

Figure S5, related to Figures 5 and 6.
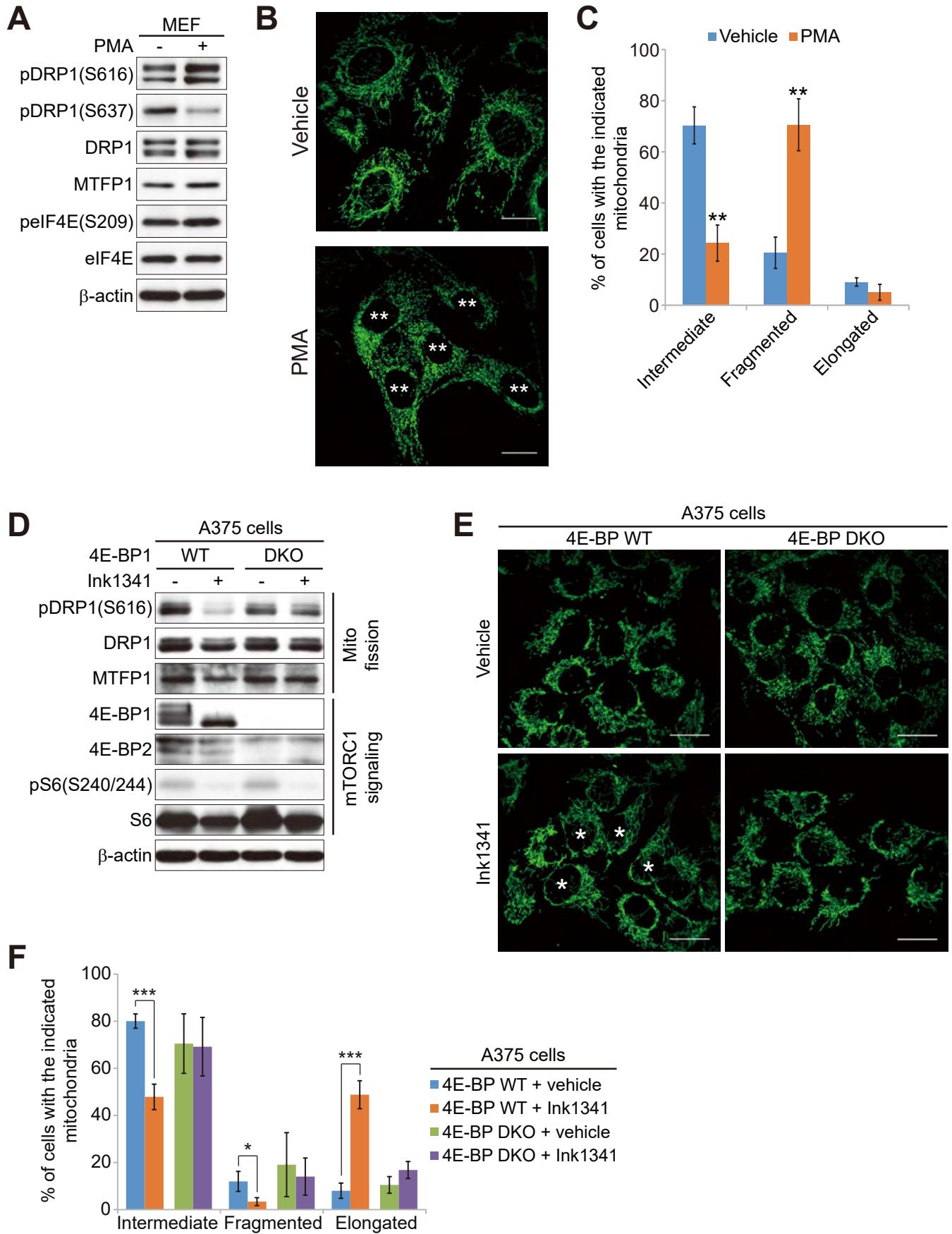
Figure S5, related to Figures 5 and 6. The 4E-BP/eIF4E pathway mediates mTORC1-dependent regulation of mitochondrial dynamics

(A) Levels of the indicated proteins in WT MEFs treated with vehicle or PMA (100 nM) for 24 hr. β-actin was used as a loading control.

(B) Representative confocal images of mitochondrial morphology in WT MEFs treated with vehicle or PMA (100 nM) for 24 hr. Mitochondria were labeled using an anti-TOM20 antibody. ** indicates cells with fragmented mitochondria. Scale bars represent 20 μm.

(C) Quantification of mitochondrial morphology in (B). n = 199 for vehicle, n = 225 for PMA from three independent experiments. Data represent mean ± SD. **P<0.01; Student's t test.

(D) Levels of the indicated proteins in 4E-BP WT and DKO A375 melanoma cells treated with vehicle or Ink1341 (200 nM) for 24 hr. β-actin was used as a loading control.

(E) Representative confocal images of mitochondrial morphology in 4E-BP WT and DKO A375 melanoma cells treated with vehicle or Ink1341 (200 nM) for 24 hr. Mitochondria were labeled using an anti-TOM20 antibody. * indicates cells with elongated mitochondria. Scale bars represent 20 μm.

(F) Quantification of mitochondrial morphology in (E). Data represent mean ± SD. n = 298 for WT + vehicle; n = 302 for WT + Ink1341; n = 372 for DKO + vehicle; n = 336 for DKO + Ink1341 from three independent experiments. . *P< 0.05, ***P< 0.001; Student's t test.

Figure S6, related to Figure 7.
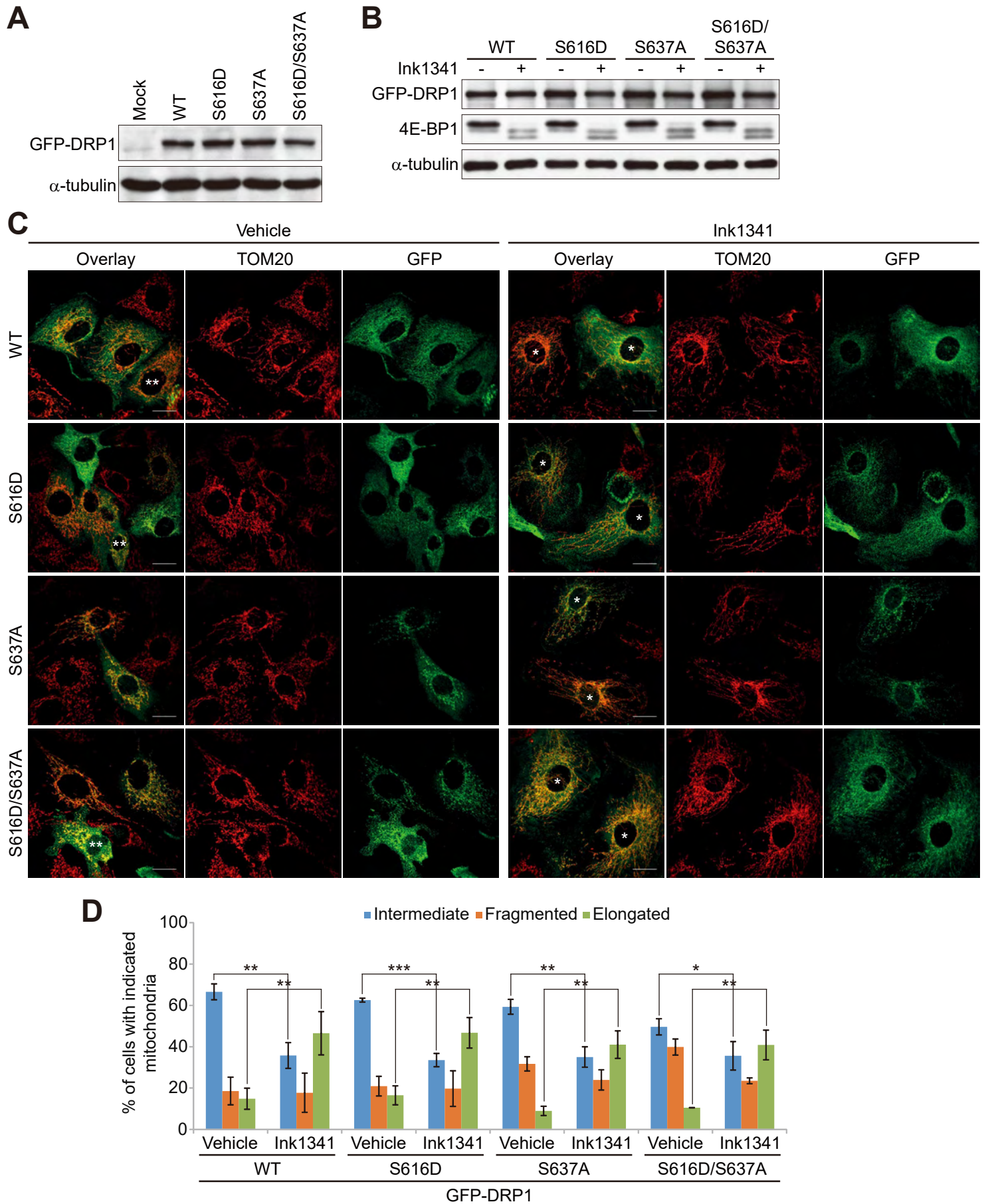
Figure S6, related to Figure 7. Effect of GFP-DRP1 phospho-mimetic/mutant overexpression on mitochondrial morphology

(A) Levels of GFP proteins in WT MEFs transiently overexpressing empty vector (Mock), GFP-DRP1-WT, -S616D, -S637A and double S616D/S637A. α-tubulin was used as a loading control.

(B) Levels of GFP-DRP1 and 4E-BP1 proteins in WT MEFs transiently overexpressing GFP-DRP1-WT, -S616D, -S637A and double S616D/S637A, treated with vehicle or Ink1341 (200 nM) for 24 hr. α-tubulin was used as a loading control.

(C) Representative confocal images of mitochondrial morphology in WT MEFs transiently overexpressing GFP-DRP1-WT, -S616D, -S637A and double S616D/S637A, treated with vehicle or Ink1341 (200 nM) for 24 hr. Mitochondria were labeled using an anti-TOM20 antibody. Scale bars represent 20 μm. * and ** indicate GFP-positive transfected cells with elongated and fragmented mitochondria, respectively.

(D) Quantification of mitochondrial morphology in (C). n = 144 for GFP-DRP1-WT + vehicle, n = 134 for GFP-DRP1-WT + Ink1341, n = 152 for GFP-DRP1-S616D + vehicle, n = 111 for GFP-DRP1-S616D + Ink1341, n = 166 for GFP-DRP1-S637A + vehicle, n = 153 for GFP-DRP1-637A + Ink1341, n = 162 for GFP-DRP1-S616D/S637A + vehicle, n = 171 for GFP-DRP1-S616D/S637A + Ink1341 from three independent experiments. Data represent mean ± SD. *$P<0.05$, **$P<0.01$, ***$P<0.001$; Student's t test.

Figure S7, related to Figure 7. MTFP1 mediates mTORC1-dependent regulation of mitochondrial dynamics and cell survival

(A) Quantification of levels of the indicated proteins in Figure 7A. Signal intensities were quantified by densitometry and normalized with a DRP1 or α-tubulin level. n = 4 per group. Data represent mean ± SEM. $*P<0.05$, $**P<0.01$; two-way ANOVA with Tukey's post-hoc test.

(B) Levels of the indicated proteins in empty vector (control) and MTFP1-overexpressing (MTFP1) raptor WT or KO MEFs. α-tubulin was used as a loading control.

(C) Representative confocal images of mitochondrial morphology in control and MTFP1-overexpressing raptor WT or KO MEFs. Mitochondria were labeled using an anti-TOM20 antibody. Scale bars represent 20 μm. * and ** indicate cells with elongated and fragmented mitochondria, respectively.

(D) Quantification of mitochondrial morphology in (C). n = 220 for raptor WT + control, n = 263 for raptor WT + MTFP1, n = 153 for raptor KO + control, n = 227 for raptor KO + MTFP1 from two independent experiments. Data represent mean ± SD. $*P<0.05$, $**P<0.01$; Student's t test.

(E) Levels of the indicated proteins in TSC2 WT and KO MEFs silenced with siRNA Control (siControl) or siRNA MTFP1 (siMTFP1). α-tubulin was used as a loading control.

(F) Representative confocal images of mitochondrial morphology in TSC2 WT and KO MEFs silenced with siControl or siMTFP1. Mitochondria were labeled using an anti-TOM20 antibody. Scale bars represent 20 μm. * and ** indicate cells with elongated and fragmented mitochondria, respectively.

(G) Quantification of mitochondrial morphology in (F). n = 218 for TSC2 WT + siControl, n = 226 for TSC2 WT + siMTFP1, n = 270 for TSC2 KO + siControl, n = 297 for TSC2 KO + siMTFP1 from three independent experiments. Data represent mean ± SD. $**P<0.01$, $***P<0.001$; Student's t test.

(H) Levels of the indicated proteins in control and MTFP1-overexpressing WT MEFs treated with vehicle or Ink1341 (200 nM) for 24 hr. β-actin was used as a loading control.

Table S1, related to Quantification and Statistical Analysis.

Figure	Parameter	N	Comparison	Statistical tests and significance
Figure 1C	Mitochondrial length	Vehicle(1544), Ink1341(987)	Vehicle vs Ink1341	Student's t-test p=1.65E-73
Figure 1D	Branched mitochondria	Vehicle(30), Ink1341(30)	Vehicle vs Ink1341	Student's t-test p=1.18E-10
Figure 1E	Mitochondrial number	Vehicle(30), Ink1341(30)	Vehicle vs Ink1341	Student's t-test p=0.0138
Figure 1F	Mitochondrial area	Vehicle(30), Ink1341(30)	Vehicle vs Ink1341	Student's t-test p=0.00441
Figure 1G	Autophagosome area	Vehicle(30), Ink1341(30)	Vehicle vs Ink1341	Student's t-test p=4.14E-05
Figure 2B	% of cells with the indicated mitochondria	Vehicle(303), Ink1341(261)	Vehicle vs Ink1341	Student's t-test; Intermediate (p<0.001), Fragmented (p<0.001), Elongated (p<0.001)
Figure 3C	% of cells with the indicated mitochondria	Raptor WT(322), KO(290)	Raptor WT vs KO	Student's t-test; Intermediate (p=0.006), Fragmented (p=0.517), Elongated (p=0.002)
		Rictor WT(347), KO(266)	Rictor WT vs KO	Student's t-test; Intermediate (p=0.644), Fragmented (p=0.803), Elongated (p=0.624)
Figure 4C	% of cells with the indicated mitochondria	TSC2 WT(191), KO(226)	TSC2 WT vs KO	Student's t-test; Intermediate (p=0.015), Fragmented (p=0.002), Elongated (p=0.002)
Figure 5C	Mitochondrial length, F=52.893, p<0.001	4E-BP WT+Vehicle(810), WT+Ink1341(504)	WT+Veh vs WT+Ink	Two-way ANOVA with Tukey's post-hoc p<0.001
		4E-BPDKO+Vehicle(691), DKO+Ink1341(719)	DKO+Veh vs DKO+Ink	Two-way ANOVA with Tukey's post-hoc p<0.001
			WT+Veh vs DKO+Veh	Two-way ANOVA with Tukey's post-hoc p=0.999
			WT+Ink vs DKO+Ink	Two-way ANOVA with Tukey's post-hoc p<0.001
Figure 5D	Branched mitochondria, F=29.996, p<0.001	4E-BP WT+Vehicle(30), WT+Ink1341(30)	WT+Veh vs WT+Ink	Two-way ANOVA with Tukey's post-hoc p<0.001
		4E-BP DKO+Vehicle(30), DKO+Ink1341(30)	DKO+Veh vs DKO+Ink	Two-way ANOVA with Tukey's post-hoc p=0.904
			WT+Veh vs DKO+Veh	Two-way ANOVA with Tukey's post-hoc p<0.001
			WT+Ink vs DKO+Ink	Two-way ANOVA with Tukey's post-hoc p=0.999
Figure 5E	Mitochondrial area, F=5.746, p=0.019	4E-BP WT+Vehicle(30), WT+Ink1341(30)	WT+Veh vs WT+Ink	Two-way ANOVA with Tukey's post-hoc p=0.034
		4E-BP DKO+Vehicle(30), DKO+Ink1341(30)	DKO+Veh vs DKO+Ink	Two-way ANOVA with Tukey's post-hoc p=0.851
			WT+Veh vs DKO+Veh	Two-way ANOVA with Tukey's post-hoc p=0.005
			WT+Ink vs DKO+Ink	Two-way ANOVA with Tukey's post-hoc p=1.000
Figure 5F	Autophagosome area, F=3.946, p=0.049	4E-BP WT+Vehicle(30), WT+Ink1341(30)	WT+Veh vs WT+Ink	Two-way ANOVA with Tukey's post-hoc p<0.001
		4E-BP DKO+Vehicle(30), DKO+Ink1341(30)	DKO+Veh vs DKO+Ink	Two-way ANOVA with Tukey's post-hoc p=0.006
			WT+Veh vs DKO+Veh	Two-way ANOVA with Tukey's post-hoc p=0.495
			WT+Ink vs DKO+Ink	Two-way ANOVA with Tukey's post-hoc p=0.601
Figure 5G	% of cells with the indicated mitochondria	4E-BP WT+Veh(333), WT+Ink1341(261)	WT+Veh vs WT+Ink	Student's t-test; Intermediate (p<0.001), Fragmented (p=0.290), Elongated (p<0.001)
		4E-BP DKO+Veh(315), DKO+Ink1341(333)	DKO+Veh vs DKO+Ink	Student's t-test; Intermediate (p=0.331), Fragmented (p=0.393), Elongated (p=0.867)
Figure 7C	% of cells with the indicated mitochondria	Cont+Veh(179), Cont+Ink1341(115)	Cont+Veh vs Cont+Ink1341	Student's t-test; Intermediate (p<0.001), Fragmented (p=0.156), Elongated (p<0.001)
		MTFP1+Veh(213), MTFP1+Ink1341(173)	MTFP1+Veh vs MTFP1+Ink1341	Student's t-test; Intermediate (p=0.051), Fragmented (p=0.663), Elongated (p=0.006)
Figure 7D	BrdU incorporation, F=39.705, p<0.001	Cont+Vehicle(5), Cont+Ink1341(5)	Cont+Veh vs Cont+Ink1341	Two-way ANOVA with Tukey's post-hoc p<0.001
		Cont+Ink128(5), MTFP1+Vehicle(5)	Cont+Veh vs Cont+Ink128	Two-way ANOVA with Tukey's post-hoc p<0.001
		MTFP1+Ink1341(5), MTFP1+Ink128(5)	MTFP1+Veh vs MTFP1+Ink1341	Two-way ANOVA with Tukey's post-hoc p<0.001
			MTFP1+Veh vs MTFP1+Ink128	Two-way ANOVA with Tukey's post-hoc p<0.001
			Cont+Ink1341 vs MTFP1+Ink1341	Two-way ANOVA with Tukey's post-hoc p=0.017
			Cont+Ink128 vs MTFP1+Ink128	Two-way ANOVA with Tukey's post-hoc p=0.022
			Cont+Veh vs MTFP1+Veh	Two-way ANOVA with Tukey's post-hoc p<0.001
Figure 7F	Caspase activity, F=1061.698, p<0.001	Cont+Vehicle(6), Cont+Ink1341(6)	Cont+Veh vs Cont+Ink1341	Two-way ANOVA with Tukey's post-hoc p<0.001
		Cont+Ink128(6), MTFP1+Vehicle(6)	Cont+Veh vs Cont+Ink128	Two-way ANOVA with Tukey's post-hoc p=0.005
		MTFP1+Ink1341(6), MTFP1+Ink128(6)	Cont+Veh vs MTFP1+Veh	Two-way ANOVA with Tukey's post-hoc p<0.001
			MTFP1+Veh vs MTFP1+Ink1341	Two-way ANOVA with Tukey's post-hoc p<0.001
			MTFP1+Veh vs MTFP1+Ink128	Two-way ANOVA with Tukey's post-hoc p<0.001
			Cont+Ink1341 vs MTFP1+Ink1341	Two-way ANOVA with Tukey's post-hoc p<0.001
			Cont+Ink128 vs MTFP1+Ink128	Two-way ANOVA with Tukey's post-hoc p<0.001
Figure S1C	Mitochondrial length	Vehicle(810), Rapamycin(506)	Vehicle vs Rapamycin	Student's t-test p=2.62E-13
	Branched mitochondria	Vehicle(30), Rapamycin(30)	Vehicle vs Rapamycin	Student's t-test p=0.628
	Mitochondrial number	Vehicle(30), Rapamycin(30)	Vehicle vs Rapamycin	Student's t-test p=0.016
	Autophagosome area	Vehicle(30), Rapamycin(30)	Vehicle vs Rapamycin	Student's t-test p=0.0147
Figure S2C	pDRP1 S616/DRP1, F=3.358, p=0.038	0 hr(4), 3 hr(4), 6 hr(4), 12 hr(4), 24 hr(4)	0 hr vs others	One-way ANOVA with Dunnett's post-hoc: 3hr(p=0.394), 6hr(p=0.026), 12hr(p=0.113), 24hr(p=0.023)
	pDRP1 S637/DRP1, F=14.321, p<0.001	0 hr(4), 3 hr(4), 6 hr(4), 12 hr(4), 24 hr(4)	0 hr vs others	One-way ANOVA with Dunnett's post-hoc: 3hr(p=0.904), 6hr(p=0.380), 12hr(p=0.002), 24hr(p<0.001)
	DRP1/Tubulin, F=2.969, p=0.054	0 hr(4), 3 hr(4), 6 hr(4), 12 hr(4), 24 hr(4)	0 hr vs others	One-way ANOVA with Dunnett's post-hoc: 3hr(p=1.000), 6hr(p=0.997), 12hr(p=0.408), 24hr(p<0.050)
	MTFP1/Tubulin, F=3.238, p=0.042	0 hr(4), 3 hr(4), 6 hr(4), 12 hr(4), 24 hr(4)	0 hr vs others	One-way ANOVA with Dunnett's post-hoc: 3hr(p=0.993), 6hr(p=0.273), 12hr(p=0.082), 24hr(p=0.039)
	OPA1/Tubulin, F=0.235, p=0.914	0 hr(4), 3 hr(4), 6 hr(4), 12 hr(4), 24 hr(4)	0 hr vs others	One-way ANOVA with Dunnett's post-hoc: 3hr(p=0.995), 6hr(p=0.772), 12hr(p=0.926), 24hr(p=0.970)
	LC3-I/Tubulin, F=6.329, p=0.003	0 hr(4), 3 hr(4), 6 hr(4), 12 hr(4), 24 hr(4)	0 hr vs others	One-way ANOVA with Dunnett's post-hoc: 3hr(p=0.011), 6hr(p=0.054), 12hr(p=0.004), 24hr(p=0.002)
	LC3-II/Tubulin, F=3.306, p=0.039	0 hr(4), 3 hr(4), 6 hr(4), 12 hr(4), 24 hr(4)	0 hr vs others	One-way ANOVA with Dunnett's post-hoc: 3hr(p=0.102), 6hr(p=0.093), 12hr(p=0.035), 24hr(p=0.016)
Figure S3C	pDRP1 S616/DRP1	Raptor WT(6), KO(6)	Raptor WT vs KO	Student's t-test P=0.014
	pDRP1 S637/DRP1	Raptor WT(6), KO(6)	Raptor WT vs KO	Student's t-test p=0.002
	DRP1/Tubulin	Raptor WT(6), KO(6)	Raptor WT vs KO	Student's t-test P=0.082
	MTFP1/Tubulin	Raptor WT(6), KO(6)	Raptor WT vs KO	Student's t-test P=4.70E-06
	OPA1/Tubulin	Raptor WT(6), KO(6)	Raptor WT vs KO	Student's t-test P=0.394
	pDRP1 S616/DRP1	Rictor WT(6), KO(6)	Rictor WT vs KO	Student's t-test P=0.318

Figure	Parameter	Groups (n)	Comparison	Statistical test
Figure S3D	pDRP1 S637/DRP1	Rictor WT(6), KO(6)	Rictor WT vs KO	Student's t-test P=0.882
	DRP1/Tubulin	Rictor WT(6), KO(6)	Rictor WT vs KO	Student's t-test P=0.426
	MTFP1/Tubulin	Rictor WT(6), KO(6)	Rictor WT vs KO	Student's t-test P=0.757
	OPA1/Tubulin	Rictor WT(6), KO(6)	Rictor WT vs KO	Student's t-test P=0.240
	pDRP1 S616/DRP1	Rictor WT(6), KO(6)	Rictor WT vs KO	Student's t-test P=0.027
	pDRP1 S637/DRP1	TSC2 WT(4), KO(4)	TSC2 WT vs KO	Student's t-test P=2.32E-05
	DRP1/Tubulin	TSC2 WT(4), KO(4)	TSC2 WT vs KO	Student's t-test P=0.034
	MTFP1/Tubulin	TSC2 WT(4), KO(4)	TSC2 WT vs KO	Student's t-test P=0.044
Figure S4C	Mitochondrial number, F=0.184, p=0.669	WT+Vehicle(30), WT+Ink1341(30)	WT+Veh vs WT+Ink	Two-way ANOVA with Tukey's post-hoc p=0.345
		DKO+Vehicle(30), DKO+Ink1341(30)	DKO+Veh vs WT+Veh	Two-way ANOVA with Tukey's post-hoc p=0.801
			WT+Ink vs DKO+Ink	Two-way ANOVA with Tukey's post-hoc p=0.861
			DKO+Veh vs DKO+Ink	Two-way ANOVA with Tukey's post-hoc p=0.412
Figure S4G	pDRP1 S616/DRP1, F=3.358, p=0.038	4E-BP WT+Vehicle(4), WT+Ink1341(4)	WT+Veh vs WT+Ink	Two-way ANOVA with Tukey's post-hoc p=0.018
		4E-BP DKO+Vehicle(4), DKO+Ink1341(4)	DKO+Veh vs WT+Veh	Two-way ANOVA with Tukey's post-hoc p>0.050
			WT+Ink vs DKO+Ink	Two-way ANOVA with Tukey's post-hoc p>0.050
			DKO+Veh vs DKO+Ink	Two-way ANOVA with Tukey's post-hoc p>0.050
	pDRP1 S637/DRP1, F=14.321, p<0.001	4E-BP WT+Vehicle(4), WT+Ink1341(4)	WT+Veh vs WT+Ink	Two-way ANOVA with Tukey's post-hoc p=0.048
		4E-BP DKO+Vehicle(4), DKO+Ink1341(4)	DKO+Veh vs WT+Veh	Two-way ANOVA with Tukey's post-hoc p>0.050
			WT+Ink vs DKO+Ink	Two-way ANOVA with Tukey's post-hoc p>0.050
			DKO+Veh vs DKO+Ink	Two-way ANOVA with Tukey's post-hoc p=0.007
	DRP1/Tubulin, F=2.969, p=0.054	4E-BP WT+Vehicle(4), WT+Ink1341(4)	WT+Veh vs WT+Ink	Two-way ANOVA with Tukey's post-hoc p=0.031
		4E-BP DKO+Vehicle(4), DKO+Ink1341(4)	DKO+Veh vs WT+Veh	Two-way ANOVA with Tukey's post-hoc p>0.050
			WT+Ink vs DKO+Ink	Two-way ANOVA with Tukey's post-hoc p>0.050
			DKO+Veh vs DKO+Ink	Two-way ANOVA with Tukey's post-hoc p>0.050
	MTFP1/Tubulin, F=3.238, p=0.042	4E-BP WT+Vehicle(4), WT+Ink1341(4)	WT+Veh vs WT+Ink	Two-way ANOVA with Tukey's post-hoc p=0.018
		4E-BP DKO+Vehicle(4), DKO+Ink1341(4)	DKO+Veh vs WT+Veh	Two-way ANOVA with Tukey's post-hoc p=0.015
			WT+Ink vs DKO+Ink	Two-way ANOVA with Tukey's post-hoc p>0.050
			DKO+Veh vs DKO+Ink	Two-way ANOVA with Tukey's post-hoc p>0.050
	OPA1/Tubulin, F=0.235, p=0.914	4E-BP WT+Vehicle(4), WT+Ink1341(4)	WT+Veh vs WT+Ink	Two-way ANOVA with Tukey's post-hoc p=0.142
		4E-BP DKO+Vehicle(4), DKO+Ink1341(4)	DKO+Veh vs WT+Veh	Two-way ANOVA with Tukey's post-hoc p>0.050
			WT+Ink vs DKO+Ink	Two-way ANOVA with Tukey's post-hoc p>0.050
			DKO+Veh vs DKO+Ink	Two-way ANOVA with Tukey's post-hoc p>0.050
	LC3-I/Tubulin, F=6.329, p=0.003	4E-BP WT+Vehicle(4), WT+Ink1341(4)	WT+Veh vs WT+Ink	Two-way ANOVA with Tukey's post-hoc p>0.050
		4E-BP DKO+Vehicle(4), DKO+Ink1341(4)	DKO+Veh vs WT+Veh	Two-way ANOVA with Tukey's post-hoc p=0.004
			WT+Ink vs DKO+Ink	Two-way ANOVA with Tukey's post-hoc p>0.050
			DKO+Veh vs DKO+Ink	Two-way ANOVA with Tukey's post-hoc p>0.050
	LC3-II/Tubulin, F=3.306, p=0.039	4E-BP WT+Vehicle(4), WT+Ink1341(4)	WT+Veh vs WT+Ink	Two-way ANOVA with Tukey's post-hoc p=0.048
		4E-BP DKO+Vehicle(4), DKO+Ink1341(4)	DKO+Veh vs WT+Veh	Two-way ANOVA with Tukey's post-hoc p>0.050
			WT+Ink vs DKO+Ink	Two-way ANOVA with Tukey's post-hoc p>0.050
			DKO+Veh vs DKO+Ink	Two-way ANOVA with Tukey's post-hoc p=0.180
Figure S5C	% of cells with the indicated mitochondria	Vehicle(199), Rapamycin(225)	Vehicle vs Rapamycin	Student's t-test; Intermediate (p=0.00139), Fragmented (p=0.0184), Elongated (p=0.001)
Figure S5F	% of A375 cells with the indicated mitochondria	4E-BP WT+Veh(298), WT+Ink1341(302)	WT+Veh vs WT+Ink	Student's t-test; Intermediate (p<0.001), Fragmented (p=0.0309), Elongated (p<0.001)
		4E-BP DKO+Veh(372), DKO+Ink1341(336)	DKO+Veh vs DKO+Ink	Student's t-test; Intermediate (p=0.905), Fragmented (p=0.697), Elongated (p=0.096)
Figure S6D	% of cells with the indicated mitochondria	DRP1-WT+Veh(144), WT+Ink1341(134)	WT+Veh vs WT+Ink1341	Student's t-test; Intermediate (p=0.00188), Fragmented (p=0.905), Elongated (p=0.009228)
		DRP1-S616D+Veh(152), S616D+Ink1341(111)	S616D+Veh vs S616D+Ink1341	Student's t-test; Intermediate (p<0.001), Fragmented (p=0.845), Elongated (p=0.00383)
		DRP1-S637A+Veh(166), S637A+Ink1342(153)	S637A+Veh vs S637A+Ink1342	Student's t-test; Intermediate (p=0.00232), Fragmented (p=0.0876), Elongated (p=0.0014)
		DRP1-SD/SA+Veh(162), SD/SA+Ink1343(171)	SD/SA+Veh vs SD/SA+Ink1343	Student's t-test; Intermediate (p=0.0373), Fragmented (p=0.00232), Elongated (p=0.00184)
Figure S7A	pDRP1 S616/DRP1, F=4.336, p=0.023	Cont+Vehicle(5), Cont+Ink1341(5)	Cont+Veh vs Cont+Ink	Two-way ANOVA with Tukey's post-hoc p=0.031
		MTFP1+Vehicle(4), MTFP1+Ink1341(4)	MTFP1+Veh vs MTFP1+Ink	Two-way ANOVA with Tukey's post-hoc p>0.050
			Cont+Ink vs MTFP1+Ink	Two-way ANOVA with Tukey's post-hoc p>0.050
			Cont+Veh vs MTFP1+Veh	Two-way ANOVA with Tukey's post-hoc p=0.442
	pDRP1 S637/DRP1, F=8.979, p=0.001	Cont+Vehicle(5), Cont+Ink1341(5)	Cont+Veh vs Cont+Ink	Two-way ANOVA with Tukey's post-hoc p=0.003
		MTFP1+Vehicle(5), MTFP1+Ink1341(5)	MTFP1+Veh vs MTFP1+Ink	Two-way ANOVA with Tukey's post-hoc p>0.050
			Cont+Ink vs MTFP1+Ink	Two-way ANOVA with Tukey's post-hoc p>0.050
			Cont+Veh vs MTFP1+Veh	Two-way ANOVA with Tukey's post-hoc p>0.050
	DRP1/Tubulin, F=15.451, p<0.001	Cont+Vehicle(5), Cont+Ink1341(5)	Cont+Veh vs Cont+Ink	Two-way ANOVA with Tukey's post-hoc p=0.004
		MTFP1+Vehicle(5), MTFP1+Ink1341(5)	MTFP1+Veh vs MTFP1+Ink	Two-way ANOVA with Tukey's post-hoc p=0.001
			Cont+Ink vs MTFP1+Ink	Two-way ANOVA with Tukey's post-hoc p>0.050
			Cont+Veh vs MTFP1+Veh	Two-way ANOVA with Tukey's post-hoc p>0.050
			Cont+Veh vs MTFP1+Veh	Two-way ANOVA with Tukey's post-hoc p>0.050
			Cont+Veh vs MTFP1+Ink	Two-way ANOVA with Tukey's post-hoc p=0.001

Table S1, related to Quantification and Statistical Analysis. Summary of statistical analysis

Movie S1, related to Figure 1. 3-D Volren of mitochondria of wild-type MEFs treated with Ink1341

FIB-SEM 3-D visualization from 30 consecutive serial sections of wild-type MEFs treated with Ink1341 (200 nM) for 24 hr.

Movie S2, related to Figure 1. 3-D Volren of mitochondria of wild-type MEFs treated with vehicle

FIB-SEM 3-D visualization from 30 consecutive serial sections of wild-type MEFs treated with vehicle for 24 hr.